# THE HYDROGEN ATOM IN A UNIFORM MAGNETIC FIELD – AN EXAMPLE OF CHAOS

**Harald FRIEDRICH**

*Technische Universität München, Physik-Department, 8046 Garching, West Germany*

and

**Dieter WINTGEN**

*Max-Planck-Institut für Kernphysik, Postfach 103980, 6900 Heidelberg, West Germany*
*and Institute for Theoretical Physics, University of California,*
*Santa Barbara, CA 93106, USA*

NORTH-HOLLAND – AMSTERDAM

PHYSICS REPORTS (Review Section of Physics Letters) 183, No. 2 (1989) 37–79. North-Holland, Amsterdam

# THE HYDROGEN ATOM IN A UNIFORM MAGNETIC FIELD – AN EXAMPLE OF CHAOS

Harald FRIEDRICH

*Technische Universität München, Physik-Department, 8046 Garching, West Germany*

and

Dieter WINTGEN

*Max-Planck-Institut für Kernphysik, Postfach 103980, 6900 Heidelberg, West Germany*
*and Institute for Theoretical Physics, University of California, Santa Barbara, CA 93106, USA*

Received May 1989

*Contents:*



*Abstract:*

The hydrogen atom in a uniform magnetic field is discussed as a real and physical example of a simple nonintegrable system. The quantum mechanical spectrum shows a region of approximate separability which breaks down as we approach the classical escape threshold. Classical dynamics depends only on the scaled energy given as the true energy divided by the third root of the square of the field strength. The classical transition from regular motion below the escape threshold to chaos near the escape threshold is accompanied by a corresponding transition in statistical properties of the short ranged quantum spectral fluctuations. Spectral properties involving correlations on a longer range depend sensitively on system-specific nonuniversal properties such as the occurrence of prominent periodic classical orbits. Knowledge of the classical periodic orbits leads to a quantitative understanding of the low frequency properties of the quantum spectra as summarized in Gutzwiller's trace formula. These developments have led to a deeper understanding of the long known "quasi-Landau resonances" and other modulations in photoabsorption spectra.

## 1. Introduction

Although the equations of motion of classical mechanics are strictly deterministic, the actual path along which a complex classical system evolves may depend extremely sensitively on the initial conditions so that the evolution of the system becomes de facto unpredictable. Such a system is said to behave irregularly or chaotically. The fact that classical motion can be irregular has been known at least since the beginning of this century. However in recent years it has become increasingly clear that even seemingly simple systems with few degrees of freedom generally show chaotic behaviour, and advances in computer technology have made it possible to study irregular motion in small systems in considerable detail. This has made chaos one of the fastest growing fields in physics.

Bound classical motion in one spatial degree of freedom is always periodic if it is governed by a time independent Hamiltonian, i.e. if energy is conserved, and hence one-dimensional conservative systems cannot be chaotic. The same is true for $N$-dimensional conservative systems, $N>1$, if they are integrable, i.e. if their Hamiltonian can be written in terms of $N$ conserved actions. The simplest conservative systems capable of exhibiting chaos are systems in $N=2$ spatial dimensions with no other integral of motion besides the energy. Examples are various types of single particle billards [1–3], the Hénon–Heiles potential [4], various types of anharmonically coupled harmonic or anharmonic oscillators [5, 6], or the problem of a hydrogen atom in a uniform magnetic field (see fig. 1).

In contrast to the other simple systems mentioned above, the hydrogen atom in a uniform magnetic field is not an abstract model system but a real physical system that can be and has been studied in the laboratory [7, 8]. When we study the regular or chaotic nature of the classical dynamics or look for manifestations of classical chaos in quantum spectra we are, in this example, doing real physics and not only mathematical physics. Our objects of study are sometimes classical trajectories or quantum spectra generated by computer codes, frequently however they are real spectra observed in experiments. In some cases, e.g. for the oscillations in photoabsorption spectra which have long been known under the name of *quasi-Landau resonances*, a deeper appreciation of the classical dynamics, and in particular of the important role of isolated unstable periodic orbits embedded in the chaotic part of the phase space, has led to a deeper understanding of the structure of complex spectra. In particular, we now understand why the experimentally observed quasi-Landau peaks are related to closed classical orbits in a way resembling a Bohr–Sommerfeld quantization condition, even in the classically chaotic region, where the orbits are unstable and the observed peaks do not correspond to individually resolved quantum states.

The aim of this article is to give a review of recent work on the hydrogen atom in a uniform magnetic field, paying special attention to the occurrence of chaos in the classical dynamics and its manifestation

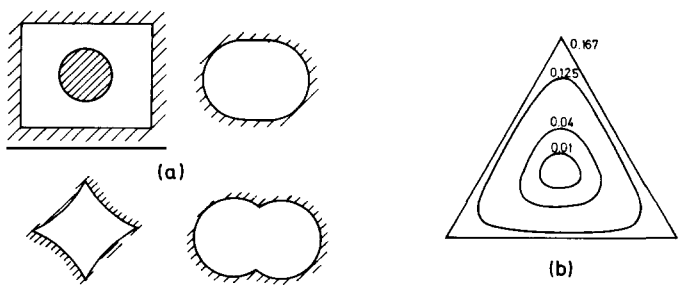


Fig. 1. (a) Examples of single particle billards showing chaotic classical dynamics; a point particle moves freely in the enclosed area and is reflected by the shaded boundaries. (b) Equipotential lines of the Hénon–Heiles potential [4].

in observed or observable quantum spectra. Chapter 2 contains a description of the system and a general discussion of the properties of its quantum mechanical spectrum, including a comparison between calculated and observed spectra. Chapter 3 contains a detailed discussion of the classical dynamics while chapter 4 discusses how the nature of the classical dynamics, in particular the occurrence of regular and chaotic motion and the existence of periodic orbits, manifests itself in the quantum spectra.

## 2. The quantum mechanical hydrogen atom in a uniform magnetic field

### 2.1. Hamiltonian

The hydrogen atom in a uniform magnetic field is accurately described over a wide range of field strengths $B$ by the simple nonrelativistic single-particle Hamiltonian

$$H = p^2/2m_e - e^2/r + \omega l_z + \tfrac{1}{2} m_e \omega^2 (x^2 + y^2) . \tag{1}$$

The direction of the field is taken as the $z$-direction and $m_e$ is the reduced mass of electron and nucleus. The frequency $\omega$ in (1) is half the cyclotron frequency

$$\omega = \tfrac{1}{2}\omega_c = eB/2m_e c . \tag{2}$$

At a field strength of

$$B = B_0 = m_e^2 e^3 c/\hbar^3 \approx 2.35 \times 10^9 \text{ G} = 2.35 \times 10^5 \text{ T} , \tag{3}$$

the oscillator energy $\hbar\omega$ equals the Rydberg energy $\mathcal{R} = m_e e^4/(2\hbar^2) \approx 13.6$ eV. In terms of the dimensionless field strength parameter

$$\gamma = B/B_0 = \hbar\omega/\mathcal{R} , \tag{4}$$

relativistic corrections [9] to the simple model defined by (1) are negligible for fields with $\gamma < 10^4$. On the other hand, the effects of spin–orbit coupling [10] can be neglected for fields with $\gamma n^3 > 10^{-4}$, where $n$ is the principal quantum number. Effects related to the two-body (nucleus and electron) center of mass motion in the presence of an external magnetic field have been investigated by several authors [10–14]. It is possible to separate a generalized field strength dependent momentum, which replaces the center of mass momentum of the field-free two-body system. For fields with $\gamma > 100$ the internal dynamics is considerably influenced by the center of mass motion, but for a vanishing transversal component of the conserved generalized momentum the effect can be accounted for accurately by a constant energy shift which depends only on the magnetic field strength and the azimuthal quantum number $m$ [13].

The azimuthal quantum number $m$ is a good quantum number as is parity, which is frequently expressed in terms of the $z$-parity $\pi$ defined with respect to reflection at the $xy$-plane which is perpendicular to the direction of the magnetic field. In each $m^\pi$ subspace of Hilbert space the Schrödinger equation defined by the Hamiltonian (1) remains nonseparable in the two coordinates $z$,

parallel, and $\rho = \sqrt{x^2 + y^2}$, perpendicular, to the field. Leaving out the contribution of the normal Zeeman term $\omega l_z$ because it is constant, the stationary Schrödinger equation in a given $m^\pi$ subspace is (in atomic units, which we will use throughout unless stated otherwise):

$$\left[\frac{1}{2}\left(-\frac{1}{\rho}\frac{\partial}{\partial\rho}\rho\frac{\partial}{\partial\rho} - \frac{\partial^2}{\partial z^2} + \frac{m^2}{\rho^2}\right) + \tfrac{1}{8}\gamma^2\rho^2 - (\rho^2 + z^2)^{-1/2}\right]\Psi(\rho, z) = E\Psi(\rho, z)\,, \tag{5}$$

where $\Psi(\rho, z)$ is the cylindrical radial part of the full single-electron wave function $\Psi$,

$$\Psi(\rho, z, \phi) = (1/\sqrt{2\pi})\Psi(\rho, z)\,\mathrm{e}^{im\phi}\,. \tag{6}$$

Thus the physical problem is that of a particle moving in an effective two-dimensional potential

$$V(\rho, z) = \tfrac{1}{8}\gamma^2\rho^2 + m^2/2\rho^2 - 1/\sqrt{\rho^2 + z^2}\,. \tag{7}$$

The potential (7) is illustrated in fig. 2 for $m = 0$.

Attempts to solve the Schrödinger equation (5) have a long history. Early accurate numerical calculations of the energies of low-lying states are due to Praddaude [15], Smith et al. [16] and Simola and Virtamo [17]. First accurate numerical calculations going beyond the lowest three or four states in each $m^\pi$ subspace were performed by Clark and Taylor [18] who calculated energies, wave functions and oscillator strengths up to and beyond the onset of the $n$-mixing regime (see section 2.2) at a field strength of $\gamma = 2 \times 10^{-5}$ (corresponding to $B = 4.7$ T).

Review articles dealing wholly or in part with the problem of a hydrogen atom in a uniform magnetic field have been written by Garstang [10], Bayfield [19], Kleppner et al. [20], Gay [21], Clark et al. [22], Delande et al. [23] and Clark [24]. Highly accurate values for the ground state energy have been given by Le Guillou and Zinn-Justin [25], and Rösner et al. [26] have given a comprehensive list of the energies of the lowest four or five states in various $m^\pi$ subspaces at arbitrary field strengths (see also Rech et al. [27], Cho et al. [28], and Liu and Starace [29]). Some recent approaches to solve the problem for Rydberg states in moderate fields involve higher order perturbation theory [30–32], diagonalization in symmetry adapted basis sets [30, 33, 34], adiabatic semiclassical methods [35, 36], and an adiabatic quantum approach [140]. At very high fields, $\gamma > 1$, the diamagnetic term proportional to $\gamma^2$ dominates the entire spectrum and convergent expansions in the Landau basis are practicable (see section 2.2). In this region complete calculations of bound states [37] and extensive studies of continuum states have been undertaken [31, 38–41].

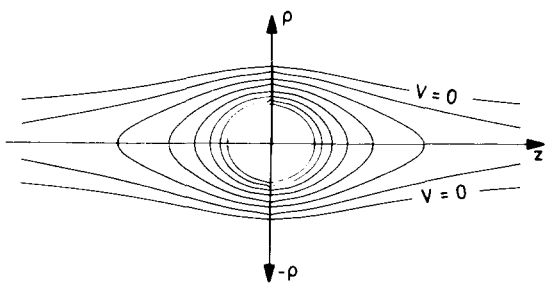


Fig. 2. Equipotential lines of the potential (7) for azimuthal quantum number $m = 0$.

### 2.2. High field and low field regime

At very high fields the Schrödinger equation (5) is best solved [15–17, 37, 38] by expanding the wave function $\Psi(\rho, z)$ in Landau states $\Phi_{Nm}(\rho)$, which are the normalized radial parts of the two-dimensional harmonic oscillator wave functions corresponding to the oscillator energy $\hbar\omega = \gamma$

$$\Psi(\rho, z) = \sum_{N \geq 0} \Phi_{Nm}(\rho)\Psi_N(z) . \tag{8}$$

This leads to a set of coupled channel equations for the wave functions $\Psi_N(z)$ in the various Landau channels:

$$\left(\frac{1}{2}\frac{d^2}{dz^2} - N\gamma + (E - E_m)\right)\Psi_N(z) - \sum_{N'} V^m_{NN'}(z)\Psi_{N'}(z) = 0 . \tag{9}$$

In (9) $E_m = (|m| + 1)\gamma/2$ is the zero-point energy of the lowest Landau state and defines the real ionization threshold in the corresponding $m^\pi$ subspace – as opposed to the *zero-field threshold* at $E = 0$ in eq. (5). The potentials in (9) are defined by

$$V^m_{NN'}(z) = \int_0^\infty d\rho\, \rho\Phi_{Nm}(\rho) \frac{-1}{\sqrt{\rho^2 + z^2}} \Phi_{N'm}(\rho) \tag{10}$$

and do not depend on the sign of the azimuthal quantum number $m$. Analytic expressions for $V^m_{NN'}(z)$ have been given by Friedrich and Chu [38]. Asymptotically (large $|z|$) the diagonal potentials are given by

$$V^m_{NN}(z) = -\frac{1}{|z|}\left(1 - \frac{2N + |m| + 1}{2}\frac{b^2}{z^2} + O(z^{-4})\right), \tag{11}$$

where $b = \sqrt{2/\gamma}$ is the oscillator width of the Landau states. An efficient numerical procedure for calculating the potentials and solving the coupled equations (9) for various magnetic field strengths can be obtained by exploiting the fact that the potentials only depend on the field strength via a universal scaling factor $1/b$ [31, 42].

The formulation (9) of the Schrödinger equation (5) shows that we have, in each $m^\pi$ subspace, a system of coupled Coulombic channels which are labelled by the Landau quantum number $N = 0, 1, 2, \ldots$. The channel thresholds

$$E_{mN} = E_m + N\gamma \tag{12}$$

lie $N\gamma$ above the real ionization threshold $E_m$ in the respective subspace. The coupling potentials $V^m_{NN'}(z)$ fall off relatively slowly and are asymptotically proportional to $z^{-2|N-N'|-1}$.

For extremely large field strengths the energy $\gamma$ needed to excite a Landau oscillation perpendicular to the magnetic field becomes very large and the problem approaches that of a one-dimensional hydrogen atom parallel to the field [43]. The bound states are then dominated by the contribution from the $N = 0$ channel, in which the motion of the electron perpendicular to the field is given by the lowest

Landau state $\Phi_{0,m}$, and they form a nondegenerate Rydberg series converging to the respective ionization threshold $E_m$ [37]

$$E_\nu = E_m - 1/2(\nu - \mu_\nu)^2 , \tag{13}$$

where $\nu$ runs from zero to infinity for positive $z$-parity states and from one to infinity for negative $z$-parity states. The *quantum defect parameters* $\mu_\nu$ in (13) are all negative and converge to zero in the limit of infinite field strengths; note that the lowest state in each $m^\pi$ subspace of positive $z$-parity corresponds to $\nu = 0$ and becomes infinitely bound in this limit.

At sufficiently high field strengths, $\gamma \gtrsim 1$, Landau excited states corresponding to $N > 0$ all lie above the ionization threshold and form Rydberg series of autoionizing resonances which converge to the respective Landau channel thresholds (12). These resonances can autoionize by de-excitation of Landau oscillations perpendicular to the field [38]. The spectrum of bound and autoionizing states in the $m^\pi = 0^+$ subspace is illustrated in fig. 3 for $\gamma = 2$, $\gamma = 1$, and $\gamma = 0.5$.

As the field strength is reduced from values around $\gamma = 1$, the Rydberg series associated with the different Landau channels begin to overlap and interfere. Near $\gamma = 0.3$ the lowest autoionizing resonances, which are characterized by a jump through $\pi$ of the asymptotic phase shift $\delta$ of the open channel ($N = 0$) wave function, cross the ionization threshold and become perturbations of the Rydberg series of bound states, which are characterized by a jump through unity of the corresponding quantum defects $\mu_\nu$. This is illustrated in fig. 4 for the $m^\pi = 0^+$ subspace. As the field strength is reduced further, more and more Rydberg series overlap and the spectrum becomes increasingly complicated. As long as not too many Rydberg series overlap, the problem may be treated with the techniques of multichannel

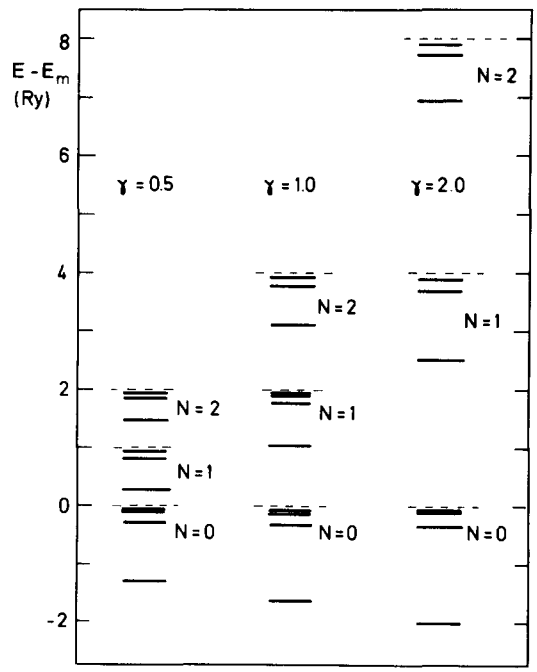


Fig. 3. Spectrum of bound and autoionizing states in the $m^\pi = 0^+$ subspace for field strength parameters $\gamma = 2.0$, 1.0, 0.5 (from ref. [42]).

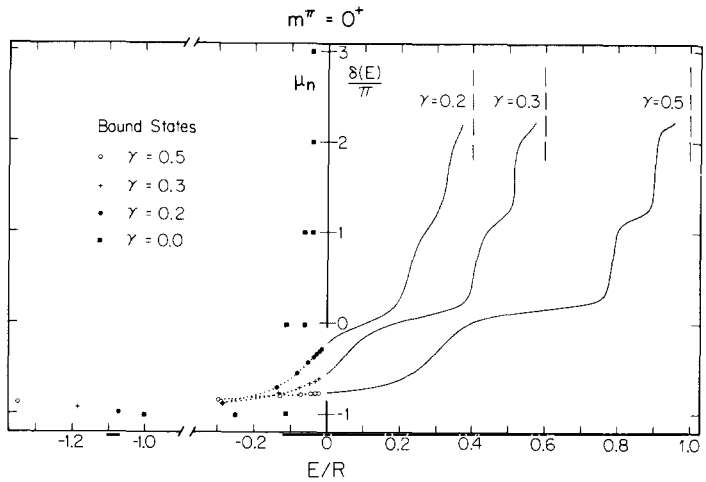


Fig. 4. Quantum defects $\mu_n$ of bound states and asymptotic phase shifts of the open channel ($N = 0$) wave function for various values of the field strength parameter $\gamma$ (from Friedrich and Chu [38]). ($E$ is the energy relative to threshold in Rydbergs.)

quantum defect theory [44, 45]. Figure 5 illustrates the multichannel structure of the spectrum in the $m^\pi = 1^+$ subspace at $\gamma = 0.04$. The top half of the figure shows the quantum defects of the bound states (left half) and the asymptotic phase shifts of the open channel ($N = 0$) wave functions in the region between the ionization threshold $E_m$ and the inelastic threshold $E_{m,N=1} = E_m + \gamma$ (right half). The perturber of the bound states and the resonances above threshold form a Rydberg series whose energies

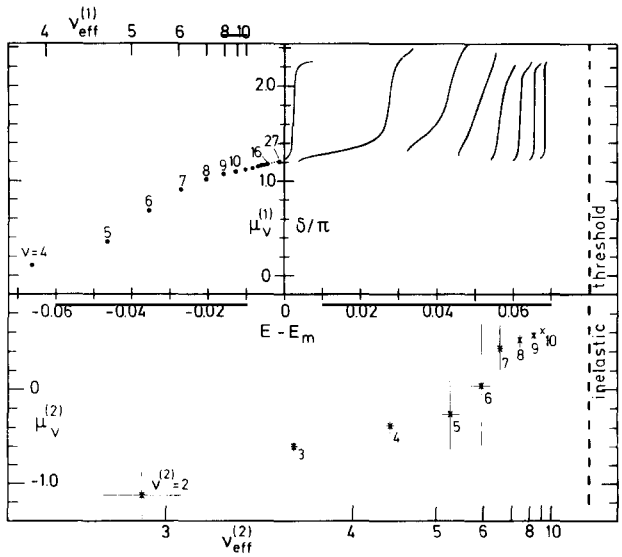


Fig. 5. Spectrum in the $m^\pi = 1^+$ subspace at $\gamma = 0.04$. The top half shows quantum defects of the perturbed Rydberg series of bound states ($E < E_m$) and the asymptotic phase shifts of the open channel ($N = 0$) wave function for energies between the ionization threshold and the inelastic threshold (first Landau threshold). The bottom half of the figure shows the quantum defects of the (perturbed) Rydberg series which consists of the bound-state perturber in the left hand part of the top half and the resonances in the right hand part of the top half. The horizontal bars show the absolute widths of the perturber and the resonances, while the vertical bars show the same widths multiplied by the third power of the effective quantum number $\nu_{eff}^{(2)}$ with respect to the inelastic threshold. These renormalized widths would be roughly constant in an unperturbed Rydberg series of autoionizing resonances. (From ref. [42].) (Energies are in Rydbergs.)

$E_\nu$ converge to the inelastic, the $N=1$, threshold and can be characterized by a series of second order quantum defects $\mu_\nu^{(2)}$:

$$E_\nu = E_{m,N=1} - 1/2(\nu^{(2)} - \mu_\nu^{(2)})^2 . \tag{14}$$

This series of perturbers and resonances is in turn perturbed by a resonance associated with the Rydberg series converging to the $N=2$ Landau channel threshold, and this affects the energies, as shown by the jump through unity of the second order quantum defects $\mu_\nu^{(2)}$ in the lower part of fig. 5, as well as the widths of the perturbers or resonances. The essential features of the spectrum at $\gamma = 0.04$ can be accurately described in the framework of three-channel quantum defect theory, the important channels being the $N=0$, $N=1$, and $N=2$ Landau channels [31, 42, 46, 47].

At still lower field strengths the number of interfering Landau channels becomes so large that a description in terms of the Landau basis (8) becomes impracticable. For low-lying bound states at low fields the spectrum is close to that of the field-free hydrogen atom and the effect of the diamagnetic interaction can be treated perturbatively [48–52].

At vanishing field strength the spectrum in each $m^\pi$ subspace is degenerate due to the O(4) symmetry of the pure Coulomb problem. This can be expressed in the conservation of the Runge–Lenz vector

$$\boldsymbol{A} = (-2\hbar^2 m_e E)^{-1/2}[(\boldsymbol{p} \times \boldsymbol{L}) - (m_e e^2/r)\boldsymbol{r}] . \tag{15}$$

For small but finite values of the field strength the quantity

$$\Sigma = 4A^2 - 5A_z^2 \tag{16}$$

is an invariant up to first order in $\gamma^2$. In the perturbative regime it is appropriate to label the eigenstates of $\Sigma$ by an index $k$ starting at $k=0$ for the maximum eigenvalue within a given $n$-manifold of states degenerate in the zero-field limit. In a given $m^\pi$ subspace $k$ runs from 0 (for $\pi = +1$) or 1 (for $\pi = -1$) to its maximum value $n - |m| - 1$ within a given $n$-manifold. For positive eigenvalues $s$ of (16) the eigenstates have approximately $O_\lambda(3)$ symmetry and are almost eigenstates of the angular momentum-type operator $\boldsymbol{\Lambda} = (A_x, A_y, l_z)$ with eigenvalues $\lambda(\lambda+1)$ of $\boldsymbol{\Lambda}^2$. These states are called *rotator states* and the eigenvalue $\lambda$ is related to the label $k$ by $\lambda = n - 1 - k$. The energy shifts of the rotator states are given approximately in the perturbative regime by [48, 51]

$$\Delta E^{\mathrm{rot}} = \tfrac{1}{16}\gamma^2 n^2(\tfrac{9}{2}\lambda(\lambda+1) + \tfrac{1}{2}n^2 - 3m^2 + \tfrac{13}{4}) . \tag{17}$$

The eigenfunctions of $\Sigma$ with negative eigenvalues $s$ have approximately $O(2)\otimes O(2)$ symmetry and can be described by a two-dimensional harmonic oscillator with anharmonic corrections. The approximate energy shifts of these *vibrational states* are, again to first order in $\gamma^2$:

$$\Delta E^{\mathrm{vib}} = \tfrac{1}{16}\gamma^2 n^2[(2\sigma + |m| + 1)2\sqrt{5}n - 3(2\sigma + |m| + 1)^2 - m^2 + 1] , \tag{18}$$

where $\sigma = 0, 1, 2, \ldots$ is given by $2\sigma = n - |m| - 1 - k$ or $2\sigma = n - |m| - 2 - k$, depending on whether $n - |m| - k$ is odd or even [48, 51]. The accuracy of the formulae (17), (18) has been tested by Wintgen and by Wunner [31, 52].

### 2.3. Regime of approximate separability

The classification of states by the principal quantum number $n$ and the "intrashell label" $k$ is definitely meaningful in the $l$-mixing regime where the diamagnetic interaction is strong enough to break rotational symmetry but still so weak that $n$-manifolds of states originating from different principal quantum numbers $n$ are separated in energy. It is not a priori clear whether such a classification remains meaningful in the $n$-mixing regime where neighbouring $n$-manifolds overlap. The onset of the $n$-mixing regime occurs, when the lowest $(k = n - |m| - 1)$ vibrator state of the $(n + 1)$-manifold meets the highest ($k = 0$ or $k = 1$) rotator state of the $n$-manifold. From the leading terms in (17) and (18) the onset of the $n$-mixing regime is given by

$$\gamma^2 n^7 = 16/5\,. \tag{19}$$

It was observed in numerical diagonalizations of the Hamiltonian (1) that near degeneracies occurred at the onset of $n$-mixing, the actual magnitudes of the avoided crossings between the lowest state of the $n + 1$ manifold and the highest state of the $n$-manifold decreasing exponentially with $n$ [53, 54]. This was interpreted as evidence for an additional hidden symmetry related to a further constant of motion and even as evidence for the existence of an approximately separable representation of the Hamiltonian. An additional (approximate) constant of motion valid for low fields was recognized by Solov'ev [48] and Herrick [51] and is given by the combination (16) of components of the Runge–Lenz vector. Solov'ev explained the small anticrossings of states as being a consequence of the fact that the states involved in the crossing are not only approximately eigenstates of the adiabatic invariant (16) with very different eigenvalues, but also correspond to different classes (rotator and vibrator) of eigenstates.

The above results stimulated an intensive search to find an approximately separable representation of the Hamiltonian. Such a representation was explicitly constructed by Wintgen and Friedrich [33] via a

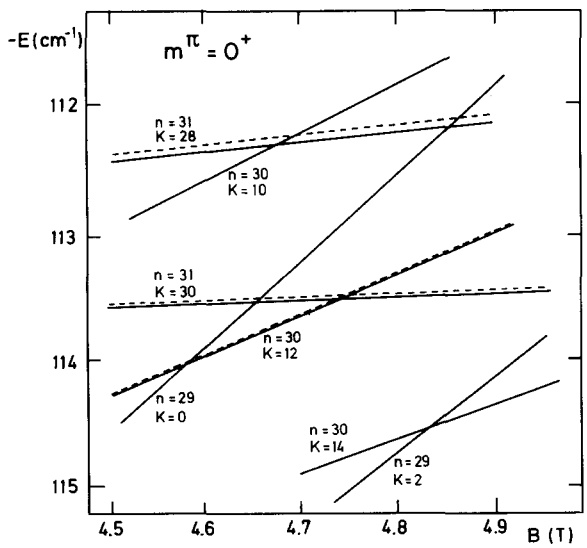


Fig. 6. Energy eigenvalues obtained by sequential diagonalization. The dashed lines show the results of diagonalizing the Hamiltonian within subspaces of states characterized by a given value of the intra-shell label $k$. The solid lines show the exact results obtained by allowing $k$-mixing. (From ref. [33].)

sequential diagonalization of the Hamiltonian, first amongst states corresponding to the same values of $k$ and subsequently including the residual interaction between states of different $k$. A natural basis for such a calculation is obtained by transforming the Schrödinger equation via the introduction of semi-parabolic coordinates into a Schrödinger equation for two azimuthally coupled harmonic oscillators (corresponding to the unperturbed Coulomb problem [55]) plus a diamagnetic potential (see [33], also Delande and Gay [50]). In this representation the matrix elements of the diamagnetic interaction depend only on the coupling constant $(\gamma/E)^2$ and not on energy and field strength independently. Matrix elements leading to $k$-mixing are very small if at least one rotator state is involved. Appreciable $k$-mixing matrix elements occur only between adjacent ($\Delta k = 2$) vibrator states. Their consideration becomes necessary when vibrator states belonging to different $n$-manifolds come close in energy. This happens near $\gamma^2 n^7 = 16$ which lies well within the $n$-mixing regime (19).

Although $k$ can no longer be simply related to an eigenvalue of the operator (16) if $n$-mixing is allowed, approximate separability and the classification according to the label $k$ remain valid well within the $n$-mixing regime. Figure 6 shows the exact eigenvalues of the Hamiltonian (solid lines) compared with the eigenvalues obtained without $k$-mixing (dashed lines) in a region of energies and field strengths corresponding to $\gamma^2 n^7 \approx 10$, which lies within the region of approximate separability. Approximate

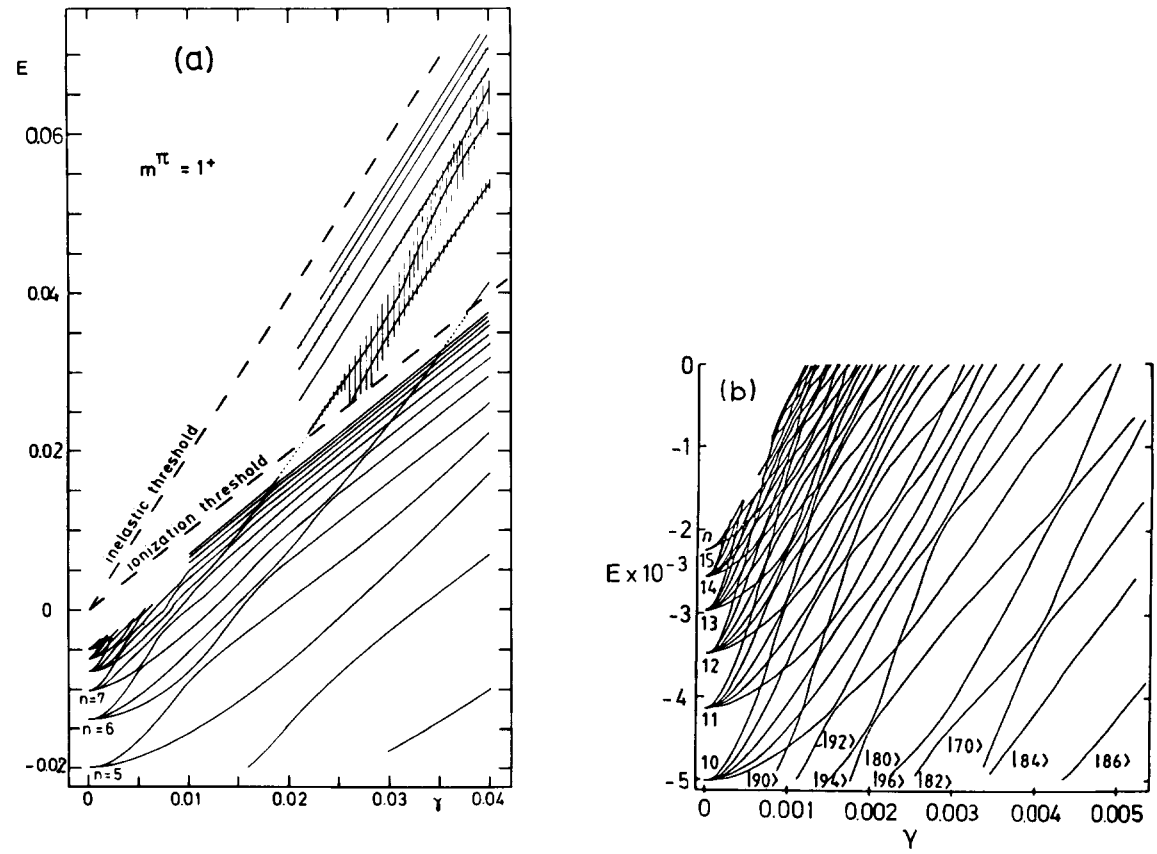


Fig. 7. (a) Overall view of the spectrum in the $m^\pi = 1^+$ subspace for arbitrary field strengths up to $\gamma = 0.04$. The vertical hatching indicates the absolute widths of the resonant states above threshold. The inelastic threshold is the Landau channel threshold corresponding to $N = 1$ (cf. eq. 12) (from ref. [42]). (b) Part of the bound state spectrum close to the zero-field threshold $E = 0$ shown on an enlarged scale, at field strengths up to $\gamma \approx 0.005$. The numbers at the bottom stand for the $n$-quantum number and the intra-shell label $k$ in the regime of approximate separability.

separability breaks down as we approach the zero-field threshold $E = 0$, where the coupling constant $(\gamma/E)^2$ determining the effective strength of the diamagnetic interaction becomes infinite.

Figure 7a shows an overall view of the spectrum in the $m^\pi = 1^+$ subspace for field strengths ranging from zero up to $\gamma = 0.04$, where the interpretation in terms of few interfering Rydberg series is valid (see fig. 5). An enlarged view of the low-field region closer to threshold is given in fig. 7b. At sufficiently low field strengths and principal quantum numbers approximate separability manifests itself in very small anticrossings of levels originating from different $n$-manifolds in the zero-field limit. For decreasing values of $E/\gamma$ increasing level repulsion associated with the breakdown of approximate separability leads to an increasingly irregular pattern and a "spaghetti"-like appearance of the spectrum.

### 2.4. *Comparison of calculated and observed spectra*

Most experimental work on Rydberg atoms in a magnetic field has concentrated on atoms more easily accessible to experiments than hydrogen [56–59]. In recent years, Welge et al. in Bielefeld have performed extensive measurements of photoabsorption cross sections of atomic hydrogen in magnetic fields up to 6 T. Because the numerical solution of the Schrödinger equation is much easier for the pure hydrogen atom, the experiments of Welge et al. have, apart from other important contributions to the central theme of this article, made a direct comparison between calculated and observed spectra possible [60, 61].

To get a feeling of the complexity of diamagnetic Rydberg spectra fig. 8 shows a part of the calculated spectrum containing states belonging to $n$-manifolds near $n = 40$ and $m^\pi = 0^+$, where high

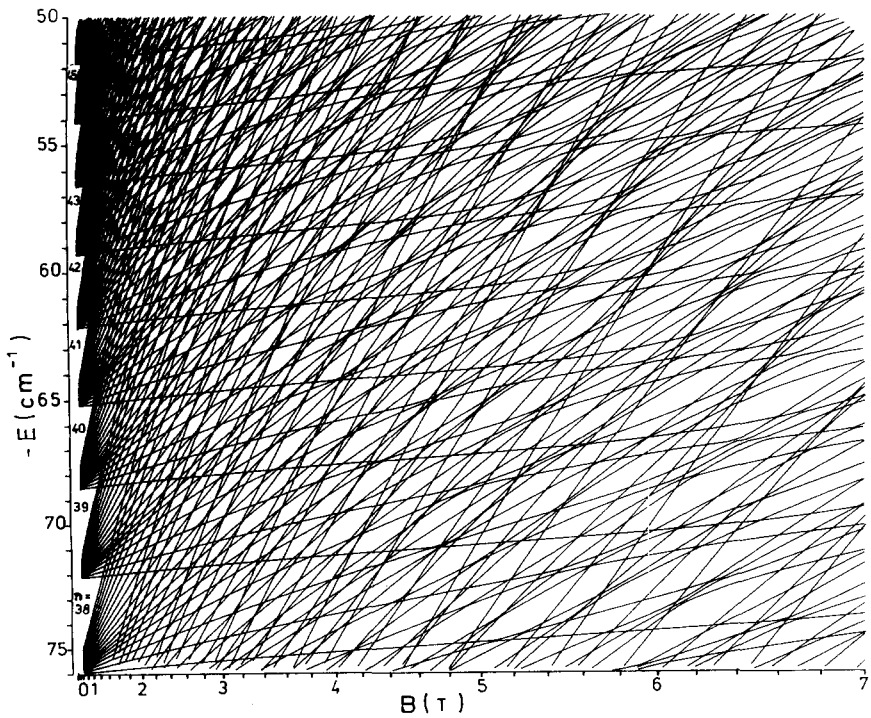


Fig. 8. Part of the bound state spectrum in the $m^\pi = 0^+$ subspace showing states from $n$-manifolds around $n \approx 40$ at field strengths up to 7 T.

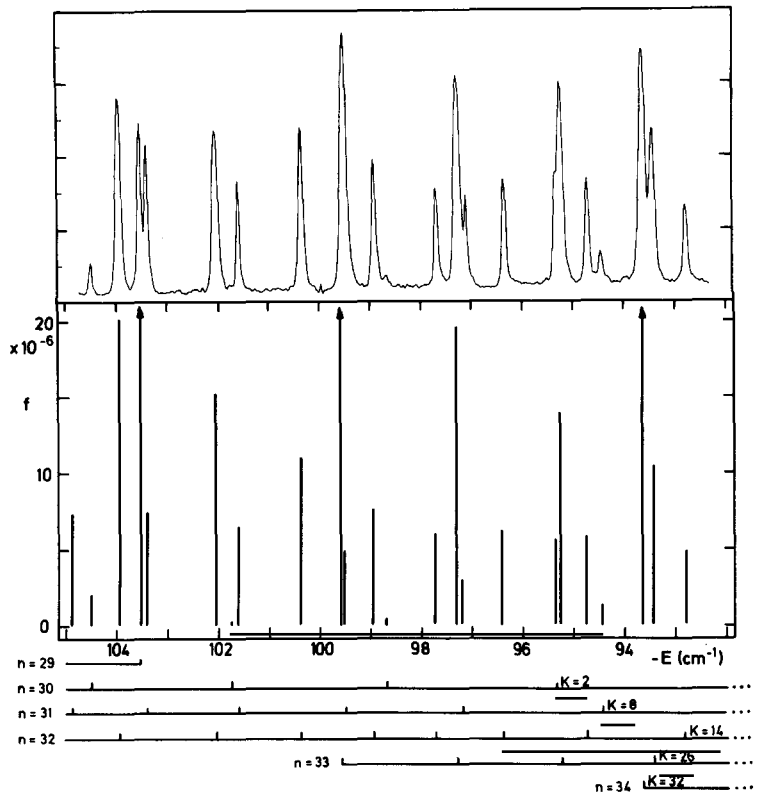


Fig. 9. Comparison of measured (top) and calculated (bottom) photoabsorption lines for $\Delta m = 0$ transitions from the $2p_{m=0}$ state into Rydberg states in the $m^{\pi} = 0^{+}$ subspace at a field strength of 6 T (from ref. [60]).

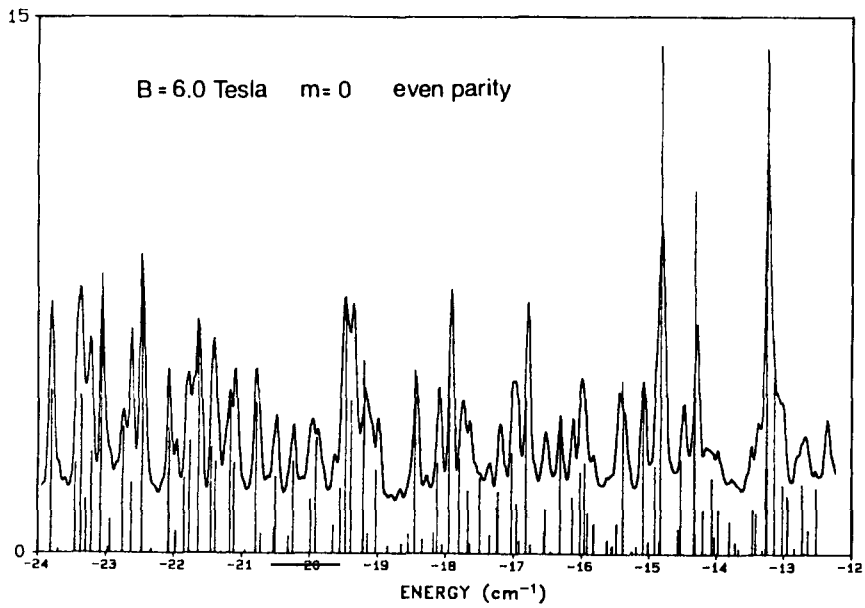


Fig. 10. Comparison of measured photoabsorption cross sections (continuous curve) with calculated photoabsorption lines for the same transitions as in fig. 9 at final state energies just below the zero-field threshold. (From Wunner et al. [61].)

resolution experiments were performed. To see many of the spectral structures the reader is invited to hold the figure very flat beneath his eyes and to turn the figure round.

Figure 9 shows a comparison of the calculated and the measured photoabsorption spectra for $\Delta m = 0$ transitions from the $2p_{m=0}$ state into the Rydberg states of the $m^{\pi} = 0^{+}$ subspace at a field strength of 6 T ($\gamma = 2.55 \times 10^{-5}$). The energy ranges up to 92 $cm^{-1}$ below the zero-field threshold, which lies well within the $n$-mixing regime but is still in the region of approximate separability, where the individual states can be unambiguously assigned two quantum numbers, $n$ (corresponding to the hydrogenic manifold from which the state evolved diabatically in the zero-field limit) and the intra-shell label $k$. Figure 10 shows a comparison of the same experimental spectrum with the final states much closer to the zero-field threshold. Figure 11 shows similar spectra for a larger range of final state energies at a slightly different field strength of 5.96 T. Figure 10 and the lower two panels in fig. 11 cover ranges of final states lying beyond the region of approximate separability and well within the "spaghetti region" (see fig. 8).

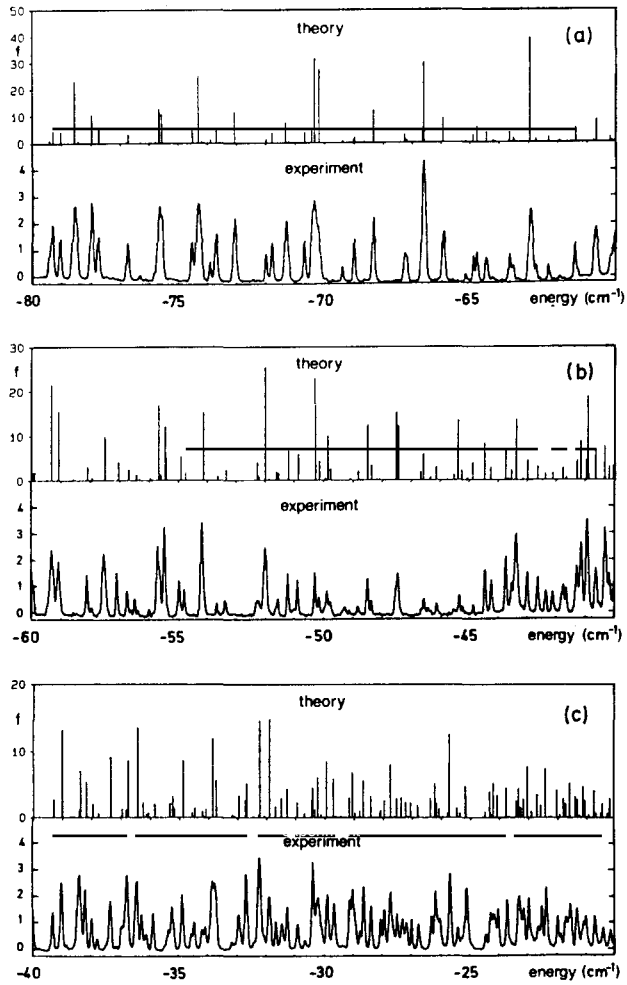


Fig. 11. Comparison of calculated (upper halves) and measured (lower halves) photoabsorption lines for the $\Delta m = 0$ transitions from the $2p_{m=0}$ state into Rydberg states in the $m^{\pi} = 0^{+}$ subspace at a field strength of 5.96 T (from Holle et al. [61]).

Most recent calculations by Zeller et al. [61] have extended the range for the spectrum at 5.96 T all the way up to the zero-field threshold $E = 0$. In all cases we observe state for state agreement between the measured and calculated spectra, at least within the limits of experimental resolution. This is of course to be expected as long as we believe that the Hamiltonian (1) accurately describes the physics of the problem and as long as we make no mistakes in measuring or calculating the spectra. Nevertheless we feel it worth pointing out that the higher lying states in figs. 10 and 11 correspond to roughly the neighbourhood of the 500th excited state in the $m^{\pi} = 0^{+}$ subspace. These are to our knowledge the most highly excited states of a measured complex spectrum that have been uniquely identified by direct comparison with an ab initio numerical calculation.

## 3. Classical dynamics

### 3.1. Scaling

The classical dynamics of the hydrogen atom in a uniform magnetic field is described by the Hamiltonian (1). In terms of the scaled coordinates and momenta

$$\tilde{\boldsymbol{r}} = \gamma^{2/3}\boldsymbol{r}\,, \qquad \tilde{\boldsymbol{p}} = \gamma^{-1/3}\boldsymbol{p}\,, \tag{20}$$

we have, in cylindrical coordinates and atomic units

$$\gamma^{-2/3}H = \tilde{H} = \tfrac{1}{2}\tilde{p}_{\rho}^{2} + \tfrac{1}{2}\tilde{p}_{z}^{2} + \tilde{l}_{z}^{2}/2\tilde{\rho}^{2} + \tfrac{1}{8}\tilde{\rho}^{2} - (\tilde{\rho}^{2} + \tilde{z}^{2})^{-1/2}\,. \tag{21}$$

Except for a similarity transformation, the classical dynamics at a given field strength $\gamma$ and energy $E$ is completely described by the Hamiltonian $\tilde{H}$. Equation (21) shows that the classical dynamics only depends on the *scaled energy* $\varepsilon$,

$$\varepsilon = E\gamma^{-2/3}\,, \tag{22}$$

and not on $E$ and $\gamma$ separately. Figure 12b shows lines of constant scaled energy next to a part of the quantum mechanical bound state spectrum in the $m^{\pi} = 1^{+}$ subspace drawn on the same scale (compare fig. 7). By keeping $\varepsilon$ constant but simultaneously changing the energy $E$ and field strength $\gamma$ we can explore different regions of the quantum spectrum without changing the structure of the underlying classical dynamics. At small (absolute) values of the energy the quantum spectrum becomes very dense, while it becomes sparse for larger field strengths and binding energies. In the $E$–$\gamma$ plane, the region close to $E = 0$, $\gamma = 0$ corresponds to a small Planck's constant $\hbar$ in comparison with typical classical actions, whereas $\hbar$ becomes effectively larger and larger as we move along lines of constant scaled energy towards larger field strengths. This can be expressed quantitatively via the commutation relations of the scaled quantum mechanical operators associated with the scaled classical variables (20), e.g.

$$[\tilde{p}_{z}, \tilde{z}] = \mathrm{i}\gamma^{1/3}\hbar\,. \tag{23}$$

At a fixed scaled energy $\varepsilon$ determining the classical mechanics the dependence of the quantum

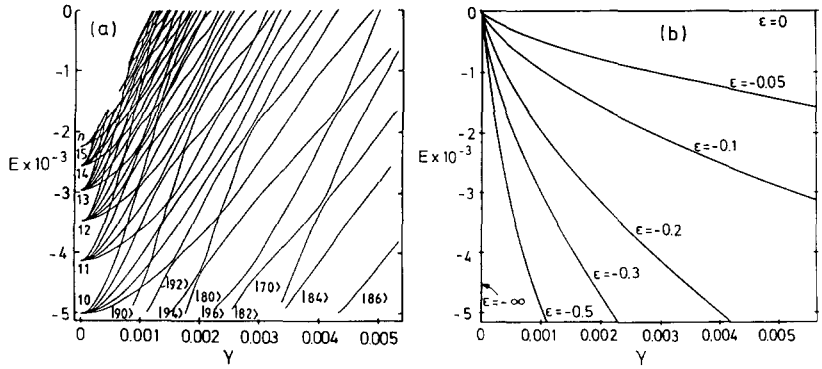


Fig. 12. (a) Part of the bound state spectrum in the $m^{\pi} = 1^{+}$ subspace previously shown in fig. 7b. (b) On the same scale, lines of constant scaled energy $\varepsilon$, along which the classical dynamics is invariant to within a similarity transformation.

mechanics on the magnetic field strength $\gamma$ can be accounted for by an effective field strength dependent Planck's constant $\gamma^{1/3}\hbar$. Keeping $\varepsilon$ constant we can study the semiclassical limit by decreasing the magnetic field strength.

### 3.2. Regularization

A feature of the Hamiltonian $\tilde{H}$ in (21) is its singularity at $\tilde{r} = 0$, which can be removed, e.g. by the introduction of semi-parabolic coordinates [62, 67]. The new coordinates $\nu$ and $\mu$ are given by

$$\nu^2 = \tilde{r} - \tilde{z}\,, \qquad \mu^2 = \tilde{r} + \tilde{z}\,, \tag{24}$$

and the momenta

$$p_\nu = \mathrm{d}\nu/\mathrm{d}\tau\,, \qquad p_\mu = \mathrm{d}\mu/\mathrm{d}\tau\,, \tag{25}$$

are defined with respect to the rescaled time $\tau$ given by:

$$\mathrm{d}t = 2\tilde{r}\,\mathrm{d}\tau = (\nu^2 + \mu^2)\,\mathrm{d}\tau\,. \tag{26}$$

The equations of motion generated by the Hamiltonian $\tilde{H}$ in (21) at a fixed value of the scaled energy are equivalent to the equations of motion generated by the Hamiltonian

$$h = \tfrac{1}{2}p_\nu^2 + l_z^2/2\nu^2 + \tfrac{1}{2}p_\mu^2 + l_z^2/2\mu^2 - \varepsilon(\nu^2 + \mu^2) + \tfrac{1}{8}\nu^2\mu^2(\nu^2 + \mu^2) \equiv 2\,, \tag{27}$$

at the fixed "pseudo energy" 2.

For negative (scaled) energies $\varepsilon < 0$ the Hamiltonian (27) represents harmonic oscillators with frequency $\omega = (-2\varepsilon)^{1/2}$, which are coupled by the term $\nu^2\mu^2(\nu^2 + \mu^2)$ originating from the diamagnetic interaction. The quadratic potential vanishes at the zero-field threshold $\varepsilon = 0$ (which is the same as the classical escape threshold for $l_z = 0$). For positive energies the Hamiltonian corresponds to inverted oscillators coupled by the diamagnetic interaction.

There is a one-to-one correspondence between the classical trajectories generated by the Hamiltonian $\tilde{H}$ (21) and $h$ (27), but they are not related by a canonical transformation. Because of the coordinate dependent rescaling of time (26), two periodic orbits which have the same period in the cylindrical representation (21) may have different periods in the semi-parabolic representation (27).

### 3.3. *Poincaré surfaces of section*

The classical dynamics of the Hamiltonian (21) has been studied by various authors in recent years [62–71]. A common way to illustrate the classical phase space structure is to look at Poincaré surfaces of section, which eliminate redundant information from classical trajectories. At a fixed (scaled) energy classical motion is confined to the *energy shell*, which is a three-dimensional subspace of the four-dimensional phase space spanned by $\nu$, $p_\nu$, $\mu$ and $p_\mu$. The Poincaré surface of section is a two-dimensional slice in the three-dimensional energy surface. The set of all intersections of a trajectory with this surface (in a certain direction) contains most of the information related to the particular trajectory. Periodic orbits are characterized by one or a finite (typically small) number $n$ of points on the surface of section, where they are called a fixed point or an $n$-cycle of the map. Regular orbits, whose motion is restricted to two-dimensional invariant manifolds (called tori) on the three-dimensional energy shell, appear as an array of dots on the surface of section, which densely fill a one-dimensional subset of the two-dimensional surface. Irregular orbits densely fill a finite volume on the three-dimensional energy shell and appear as irregularly but roughly uniformly spattered areas on the surface of section.

For $l_z = 0$ fig. 13 shows, in semi-parabolic representation, Poincaré surfaces of section for the hydrogen atom in a uniform magnetic field for six different values of the scaled energy $\varepsilon$: $-0.8$, $-0.5$, $-0.4$, $-0.3$, $-0.2$, and $-0.1$ (from left to right and top to bottom). The surface of section is defined by $\mu = 0$; the energy shell for $\mu = 0$ maps into an area bounded by the condition $-2\varepsilon\nu^2 + p_\nu^2 = 4$, which defines a circle of radius 2 with respect to the coordinates $\sqrt{-2\varepsilon}\nu$ and $p_\nu$. Time-reversal and reflection symmetry allow us to derive from each point on the surface of section three related ones, compactly written as $(\pm\sqrt{-2\varepsilon}\nu, \pm p_\nu)$.*)

At $\varepsilon = -0.8$ the system is still very close to its integrable limit $\varepsilon \to -\infty$, which corresponds to the infinitesimally perturbed hydrogen atom: all orbits are regular and confined to tori which are characterized by a specific value of the adiabatic invariant**) $\Sigma$, eq. (16). Note that even an infinitesimal perturbation is strong enough to change the phase space structure of the hydrogen atom completely. For a pure hydrogen atom the surface of section would simply give concentric circles and each orbit would contribute with a fixed point. This reflects the unusual classical behaviour of a hydrogen atom, where all orbits are periodic and degenerate in period and action. As a consequence the KAM-theorem [72, 73] is *not* applicable and in fact, little is known about the behaviour of a hydrogen atom under small perturbations. It is not self-evident that the system behaves regularly under the diamagnetic perturbation.†)

*) There is still another symmetry of the system, namely the exchange symmetry of $\nu$ and $\mu$. This can be used in numerical calculations to increase the number of sections and to accelerate the calculations.

**) Strictly speaking this is not correct, because generally tori having a rational winding number are replaced, even under an infinitesimal perturbation, by a stable $n$-cycle surrounded by elliptic islands and an unstable $n$-cycle embedded in a stochastic layer. However, the widths of the layers become infinitesimally small and hence invisible in numerical calculations when we approach the integrable limit.

†) The anisotropic Kepler problem [74, 75] provides an example, where the hydrogen atom becomes chaotic even under a very small perturbation.

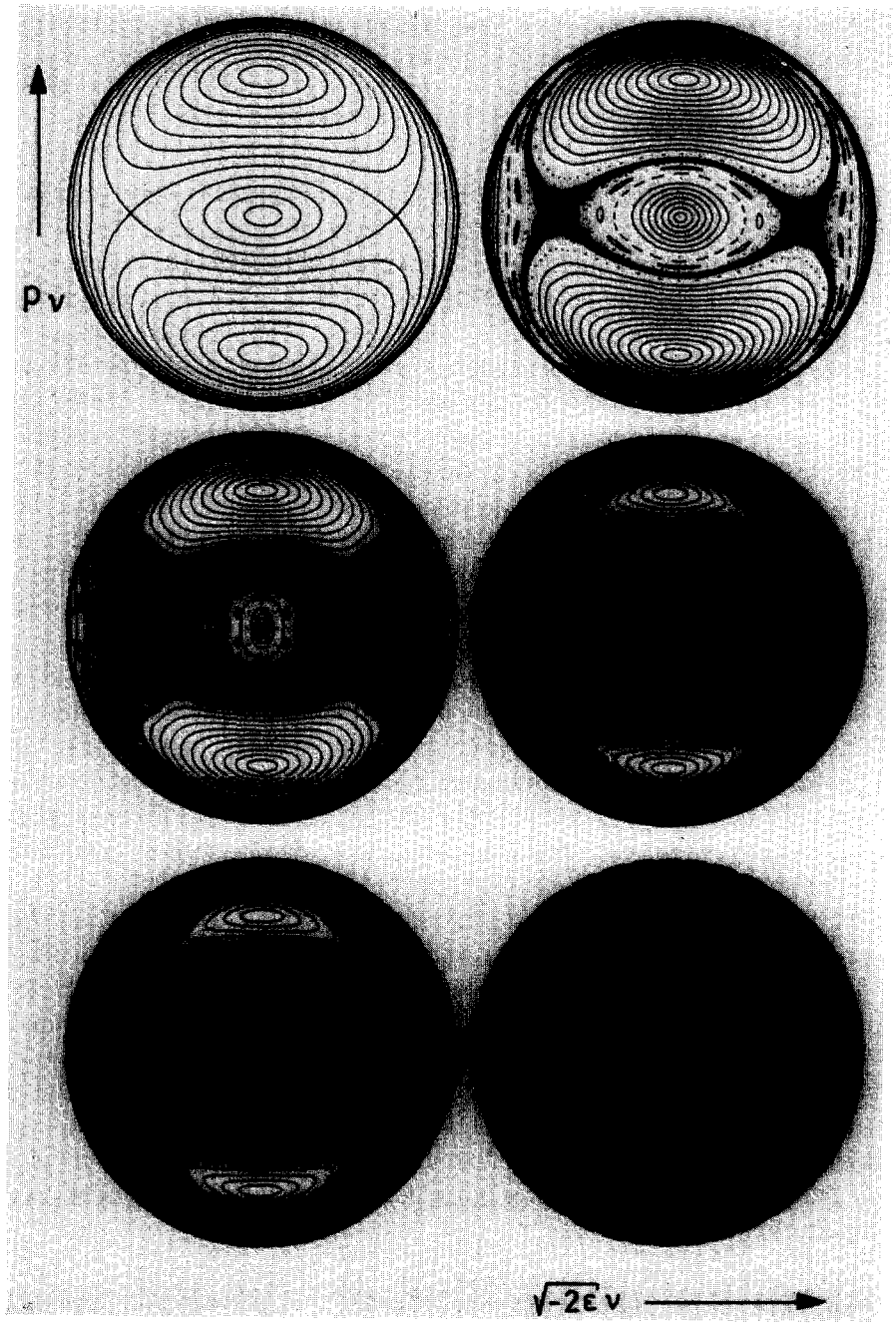


Fig. 13. Poincaré surfaces of section at $\varepsilon = -0.8$, $-0.5$, $-0.4$, $-0.3$, $-0.2$ and $-0.1$ (from left to right and top to bottom). The sections are the $\nu$–$p_\nu$ planes defined by $\mu = 0$. Horizontal axes measure $\sqrt{-2\varepsilon}\nu$, vertical axes measure $p_\nu$; the radius of the circles is 2.

The Poincaré surface of section for $\varepsilon = -0.8$ shows three important structures. The elliptic fixed point in the center of the surface of section, $\nu = p_\nu = 0$, corresponds to the $\rho \equiv 0$ straight line periodic orbit parallel to the field. The ellipses around this fixed point belong to quasiperiodic vibrational motion. These are separated from quasiperiodic rotational motion represented by the ellipses around the fixed point in the upper and lower parts of the section. The positions of these two fixed points are independent of $\varepsilon$ and are given by $(0, \pm\sqrt{2})$; they belong to the $z \equiv 0$ straight line periodic motion perpendicular to the field. The separatrix dividing these two regions of motion accumulates in a hyperbolic fixed point located at $(\pm\sqrt{2}, 0)$ (for $\varepsilon = -\infty$), which corresponds to the exactly circular orbit in the limit $\varepsilon \to -\infty$. For historical reasons the straight line orbits perpendicular and parallel to the direction of the magnetic field have come to be called $I_1$ and $I_\infty$ respectively. The almost circular orbit is labelled $C$. The labelling of rotating and vibrating motion becomes clear when we transform the phase space portrait plotted for $\varepsilon = -0.8$ in the $(\sqrt{-2\varepsilon}\nu, p_\nu)$-coordinates into a "spherical" representation defined by the radius $R^2 = p_\nu^2 - 2\varepsilon\nu^2$ (which actually corresponds to the pseudoenergy of the $\nu$-oscillator, see e.g. Delande and Gay [76]) and the angle $\phi = \arctan p_\nu/(\sqrt{-2\varepsilon}\nu)$. Such a representation is given in fig. 14, which actually shows the same phase space structure as a physical pendulum with its vibrating and rotating modes (see, e.g. ref. [73], p. 25).

As we increase the scaled energy $\varepsilon$, irregular motion appears first near the separatrix, as is clearly visible in fig. 13 for $\varepsilon = -0.5$. The separatrix is replaced by a stochastic layer, which fills a finite area in the surface of section. As we further increase the scaled energy, this layer increases in size whereas the large islands related to rotating and vibrating regular motion become smaller and smaller. Some new island structures embedded in the stochastic layer appear close to the large islands, but they disappear quickly as $\varepsilon$ is further increased. Finally, for $\varepsilon = -0.1$, no regular structure is visible on the surface of section and the classical motion is dominated by global chaos. Some regular motion is present even for $\varepsilon > -0.1$ (see section 3.4), but the related elliptic islands are so small that they are not visible on the scale of fig. 13 and their actual overall size can be neglected for our purpose.

Harada and Hasegawa [65] numerically measured the fraction of available phase space (i.e. the size of the layer in fig. 13) in which the classical trajectories are irregular. The result is plotted in fig. 15. Virtually, all of the phase space is regular for scaled energies below $\varepsilon = -0.6$. Around $\varepsilon = -0.35$ there is a rather sudden decrease to zero in the regular fraction of phase space.

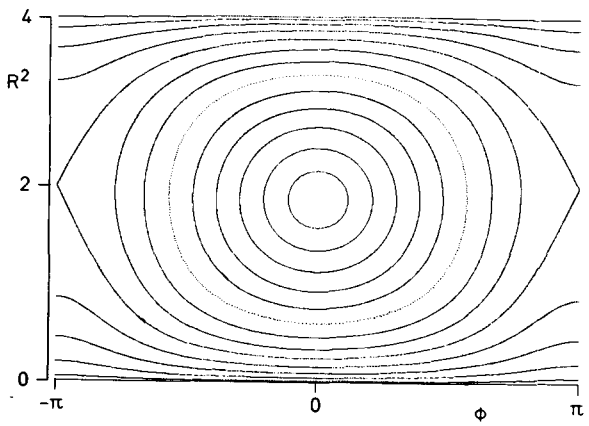


Fig. 14. Poincaré surface of section in a "spherical" representation at $\varepsilon = -0.8$.

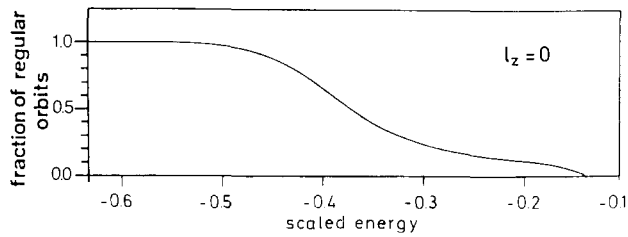


Fig. 15. Fraction of regular orbits in the surface of section as a function of scaled energy.

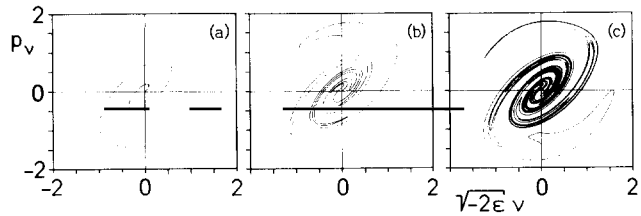


Fig. 16. Image of the interval defined by $\nu \equiv 0$, $0 \le p_\nu \le \sqrt{2}$ after (a) one, (b) two, and (c) three recurrences to the $\mu = 0$ surface.

While fig. 13 shows the long time behaviour of a few trajectories (the surface of section for $\varepsilon = -0.1$ was e.g. obtained by integrating a single trajectory for a long time), fig. 16 shows the short time behaviour of a bunch of trajectories. Here the trajectories starting on the line defined by $\nu \equiv 0$, $0 \le p_\nu \le \sqrt{2}$ in the $\mu = 0$ surface are followed up to one (a), two (b) and three (c) recurrences to the $\mu = 0$ section surface. While the single iteration structure (a) is still relatively simple, the double iteration (b) is already rather complex and the structure is completely unsurveyable after three iterations (c). Figure 16c demonstrates the build-up of a self-similar structure with increasing iteration depth. The multiply intertwined loops in a comparatively small region of phase space are responsible for the extremely sensitive dependence of the classical motion on the initial conditions: a small deviation in phase space can lead us from one loop to a neighbouring loop so that e.g. reversing the motion can lead us to widely separated points in phase space.

### *3.4. Liapunov exponents, periodic orbits and bifurcations*

One quantitative measure for the degree of chaoticity of an irregular classical orbit is its Liapunov exponent, which characterizes the rapidity of exponential divergence of nearby trajectories. A practicable way of calculating Liapunov exponents is via the stability matrix as described by Meyer [77]. For Hamiltonian flow in $N$ spatial dimensions the stability matrix $M(t_1, t_2)$ is a $2N \times 2N$ matrix which governs the infinitesimal deviations $\Delta x(t_2)$ from a given orbit in phase space at time $t_2$ as a function of arbitrary initial infinitesimal deviations $\Delta x(t_1)$ at time $t_1$: $\Delta x(t_2) = M\,\Delta x(t_1)$. The Liapunov exponent $\lambda$ is defined via the norm (any norm) $\mu(t_1, t_2)$ of $M(t_1, t_2)$

$$\lambda = \lim_{t_2 \to \infty} \frac{1}{t_2 - t_1} \ln \mu(t_1, t_2)\,. \tag{28}$$

The stability matrix obeys the differential equation

$$\dot{M} = J \frac{\partial^2 H}{\partial x^2} M , \qquad M(t, t) = 1 , \quad J = \begin{pmatrix} 0 & 1 \\ -1 & 0 \end{pmatrix}, \tag{29}$$

which can be solved numerically in the general case and almost analytically if the potential in the Hamiltonian has a simple analytic form [69, 77, 126].

The Liapunov exponent defined by eq. (28) is a unique function of the classical trajectory, i.e. all points lying on a given trajectory have the same Liapunov exponent. It is particularly easy to calculate for periodic trajectories, which only have to be followed for one period $T$. As the stability matrix $M(0, T)$ is symplectic, its eigenvalues occur in pairs of product unity – they are either complex conjugate pairs on the unit circle or a real number together with its inverse. If $\beta$ is the eigenvalue of $M(0, T)$ with the maximum absolute value, then the Liapunov exponent of the periodic orbit is given by [69]

$$\lambda = \ln(|\beta|)/T . \tag{28a}$$

For a stable periodic orbit $\lambda = 0$ the eigenvalue $\beta$ is a complex number, $\beta = \exp(2\pi i \nu_w)$. The winding number $\nu_w$ is the frequency ratio with which neighbouring trajectories wind around the periodic orbit in phase space. A stable orbit appears as an elliptic fixed point in a Poincaré surface of section. If $\lambda > 0$ the orbit is unstable and appears as a hyperbolic fixed point in the surface of section. For positive eigenvalues $\beta > 1$ we have an ordinary hyperbolic fixed point; for negative eigenvalues $\beta < -1$ the fixed point is called *inverse hyperbolic* or a hyperbolic fixed point with reflection.

The Liapunov exponent of the straight-line orbit $I_1$ perpendicular to the direction of the magnetic field is illustrated in fig. 17 as a function of the scaled energy. This orbit is stable (vanishing Liapunov exponent) for energies below $\varepsilon_0 = -0.127\,268\,612$. At this value of the scaled energy the last islands of stability still visible at $\varepsilon = -0.2$ in fig. 13 vanish and global chaos sets in. The product of the Liapunov exponent $\lambda$ and the period $T$ of the orbit then grows proportional to the square root of $(\varepsilon - \varepsilon_0)$ [68],

$$\Lambda^2 = \lambda^2 T^2 \approx 13.53(\varepsilon - \varepsilon_0) . \tag{30}$$

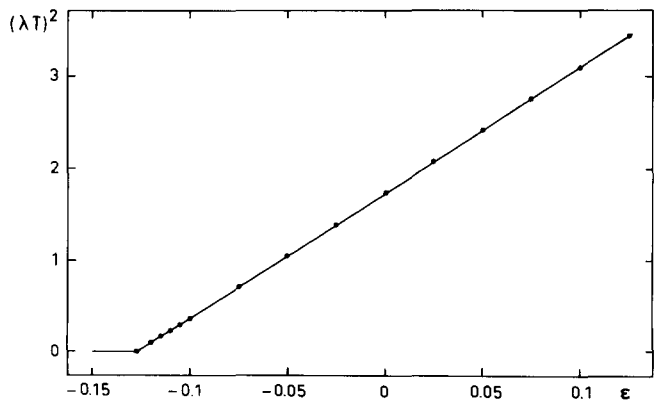


Fig. 17. Liapunov exponent $\lambda$ (multiplied by the period $T$) for the periodic straight line orbit perpendicular to the field as a function of the scaled energy (from ref. [68]).

At $\varepsilon = 0$ formula (30) yields $\Lambda = 1.312$, which should be compared with the exact value $\Lambda = 1.317 = \operatorname{arcosh}(2)$. For very large values of the scaled energy ($\varepsilon \gg 1$) $\Lambda$ increases logarithmically with $\varepsilon$ [136]. The product $\Lambda = \lambda T$ gives the rate of exponential divergence of neighbouring trajectories in units of the period of the orbit and is the Liapunov exponent of the fixed point generated by the surface of section map of the periodic orbit. In contrast to the Liapunov exponent $\lambda$ of the orbit, $\Lambda$ is an invariant property of the orbit and does not depend on whether the cylindrical or the semi-parabolic representation is used for the evolution of the classical trajectories.

Figure 18 shows the Liapunov exponent of the periodic orbit $I_\infty$ parallel to the direction of the magnetic field. This orbit is stable for scaled energies below $\varepsilon_\infty = -0.391\,300\,824$ and then goes through a sequence of intervals alternating between stability and instability [68, 69, 71]. At the points, where $I_\infty$ becomes unstable, the orbit undergoes a bifurcation and gives birth to a series of non-straight-line orbits, which were identified by Welge and collaborators [7, 8] and Al-Laithy et al. [70] and have been labelled $I_2, I_3, I_4, \ldots$ (see also refs. [62, 67]). As the energy increases, more and more of these orbits corresponding to more and more oscillations around the axis parallel to the field are born, and at the escape threshold $\varepsilon = 0$ there is an infinite sequence of such orbits [68]. The first five orbits of the series at the threshold are shown in fig. 19. The straight-line trajectory $I_\infty$ ceases to be a periodic orbit above the escape threshold, where it becomes an ionizing trajectory. The orbits $I_2, I_3, I_4, \ldots$ are born stable, but they soon become unstable and their Liapunov exponents increase monotonically with energy. The energy dependence of the Liapunov exponents is illustrated in fig. 20. The points at which the orbits $I_2$, $I_3, I_4, \ldots$ become unstable correspond to bifurcation points where stable orbits are born. These orbits do not have the symmetry of the series $I_2, I_3, I_4, \ldots$ and no longer pass through the origin. The points at which the straight line orbit $I_\infty$ regains stability are bifurcation points at which unstable orbits are born. A detailed description of the different possible scenarios of the birth (and death) of periodic orbits at points of bifurcation or confluence is given in ref. [78].

In a chaotic system the Liapunov exponents (28) of the periodic orbits fluctuate around a mean value, which is called the metric entropy $h_m$ of the system. This entropy is equal to or larger than the topological entropy $h_t$, which determines the proliferation of periodic orbits as a function of their periods; the number $N(T < T_0)$ of orbits with periods less than $T_0$ increases roughly proportional to

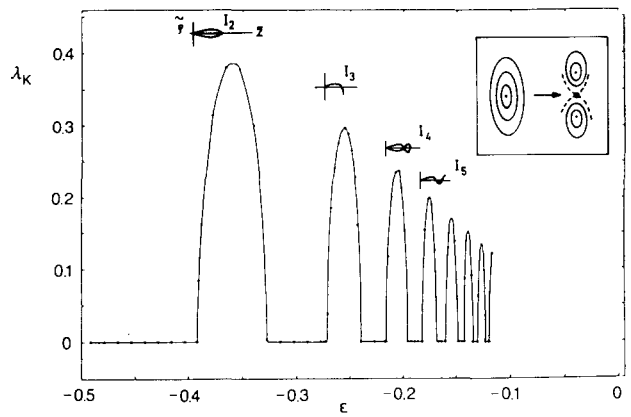


Fig. 18. Liapunov exponent $\lambda_K$ (calculated in the cylindrical representation, which describes Kepler ellipses in the zero-field limit) of the periodic orbit parallel to the magnetic field as function of scaled energy. The orbit repeatedly becomes unstable at points of bifurcation, where stable nonstraight-line orbits (corresponding to elliptical fixed points shown schematically in the inset) are born.

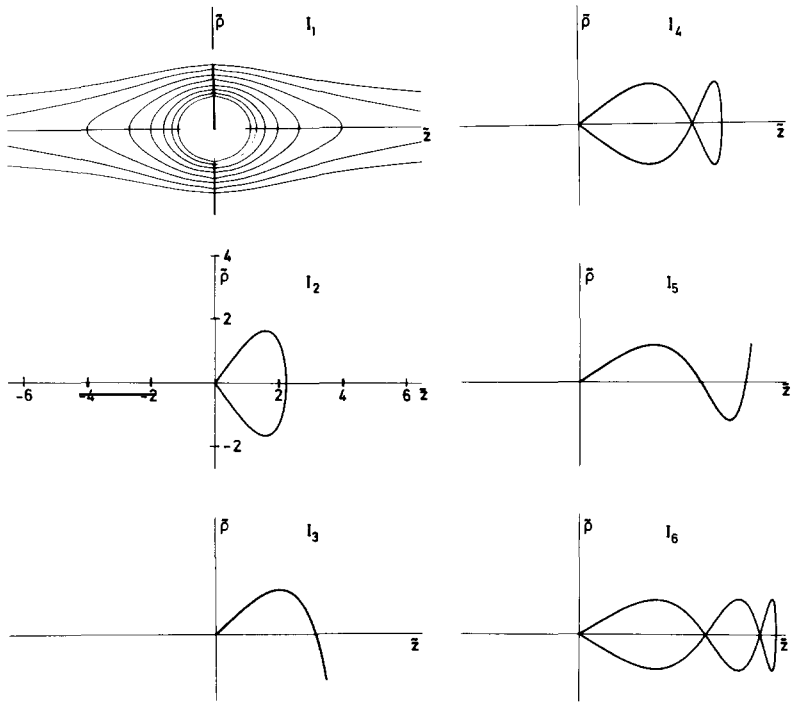


Fig. 19. Straight line orbit $I_1$ perpendicular to the direction of the field and the first five nonstraight-line periodic orbits $I_2, I_3, \ldots$ which are born out of bifurcations of the orbit $I_\infty$ parallel to the field. This figure shows the shapes of the orbits at the escape threshold $\varepsilon = 0$.

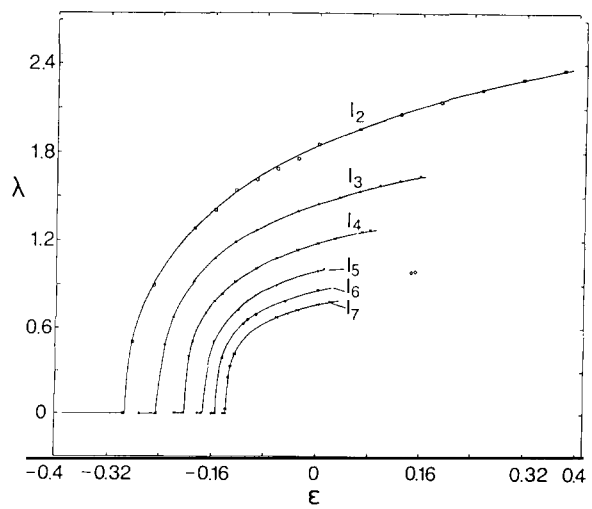


Fig. 20. Liapunov exponents (calculated in cylindrical representation) of the first six orbits of the series $I_2, I_3, \ldots$ shown in fig. 19. (From ref. [69].)

$\exp(h_t T_0)/T_0$ [79]. This is illustrated in fig. 21. For reasons discussed in section 4.4 below, it is appropriate in the present case, where the classical dynamics is determined by the scaled energy $\varepsilon$, to order the periodic orbits not by their periods $T$ but by their (scaled) actions $\tilde{S}(\varepsilon)$ defined in eq. (42). Figure 21a shows, for $\varepsilon = -0.2$, the Liapunov exponents $\Lambda = \lambda T$ for 132 primitive periodic orbits plotted against their scaled action $\tilde{S}$. (A "primitive" periodic orbit is a periodic orbit which is not a repetition of a shorter periodic orbit.) The figure includes periodic orbits with actions up to $\tilde{S} = 6$. In order to simplify the search for periodic orbits, we have confined out investigation to one-parameter families by requiring the periodic orbits to obey at least one of the following symmetries: (i) they pass through the origin, (ii) they pass perpendicularly through one of the three symmetry axes, $\nu = 0$, $\mu = 0$ or $\nu = \mu$, and (iii) they are selfretracing orbits (that is $p_\nu = p_\mu = 0$ somewhere). Figure 21a shows that there are two stable periodic orbits having a vanishing Liapunov exponent, but 130 unstable periodic orbits. The fact that there are so many unstable periodic orbits is related to their exponential proliferation in the chaotic part of the phase space (note that the fraction of the regular part of the phase space is much larger than the fraction of regular orbits 2/132, see figs. 13 and 15). From fig. 21a we estimate the average Liapunov exponent $\langle \Lambda \rangle$ of unstable periodic orbits to be approximately 1.2 times their action; thus the entropy $h_m$ is roughly unity. Although the orbits plotted in fig. 21a certainly do not cover all the primitive periodic orbits of the system up to $\tilde{S} = 6$, one can expect that these orbits have the same proliferation as all orbits together. Their proliferation is shown in fig. 21b, which gives the number of orbits with at least one of the above symmetry properties. Note that in the dense part of the figure their number increases exponentially with a slope compatible to the value of the metric entropy $h_m$.

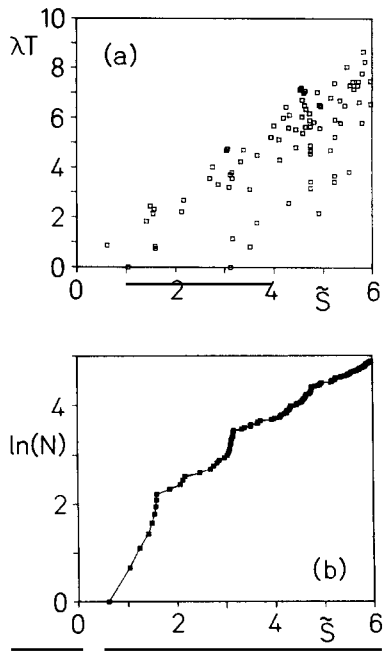


Fig. 21. (a) Liapunov exponents and (b) number $N$ of periodic orbits at a scaled energy of $\varepsilon = -0.2$ plotted against their scaled actions $\tilde{S}$ [see eq. (42) in the text] for values of $\tilde{S}$ up to six.

## 4. Quantum mechanical observables and chaos

### 4.1. General remarks on quantum chaos

In contrast to the unambiguous characterization of chaos in classical mechanics, it is as yet not clear, how the concept of chaos is to be sensibly applied in quantum mechanics. A direct transposition of the concept of diverging trajectories to quantum mechanics is impossible, because trajectories can only be defined approximately within the uncertainty governed by Planck's constant.

The role of Planck's constant in stifling chaos, or at least our classical notion of chaos, can be illustrated with the help of fig. 12. Fig. 12b shows the lines of constant scaled energy along which the classical dynamics is the same to within a trivial similarity transformation. Moving along these lines towards higher field strengths $\gamma$, i.e. towards a larger effective Planck's constant $\gamma^{1/3}\hbar$ (see eq. 23), the quantum spectrum becomes sparser and sparser until we are left with only one bound state corresponding to the zero-point motion of the electron in the two-dimensional potential illustrated in fig. 2. This happens not only for negative (scaled) energies but also around the zero-field threshold, where the classical dynamics is definitely chaotic, and even for arbitrary positive energies $\varepsilon$. The reason for this is that the real ionization threshold $E_m = (|m| + 1)\gamma/2$ (see section 2.2) increases more rapidly than the energy $E = \gamma^{2/3}\varepsilon$ along lines of fixed scaled energy $\varepsilon$, and $E$ drops below the real threshold at $\gamma = [2\varepsilon/(|m| + 1)]^3$. Since the binding energy of the ground state in a given $m^\pi$ subspace, i.e. its separation from the real ionization threshold, increases at most logarithmically with $\gamma$ [15, 25, 26], there is, for each value of the scaled energy $\varepsilon$, a critical field strength (depending on $m^\pi$ and $\varepsilon$) at which the energy $E$ equals the zero-point energy in the respective $m^\pi$ subspace. (There are no bound states at higher field strengths.) Such a single bound state has little to do with our classical notion of chaos.

At the other end, towards lower field strengths and a smaller effective Planck's constant, the spectrum becomes increasingly dense and complicated. In this region it is possible and worthwhile to study the dependence of the very complex spectra and other quantum mechanical observables on the scaled energy and to look for the manifestation of classical chaos in quantum mechanics.

### 4.2. Energy level statistics

Many model calculations have, in recent years, shown that the regular or chaotic nature of the classical dynamics of a bound system manifests itself in the statistical properties of the energy level spectrum [80–85]. Energy spectra can be expressed in terms of the spectral staircase function $N(E)$ defined by

$$N(E) = \sum_n \Theta(E - E_n) . \tag{31}$$

The properties of the spectrum are divided into a smooth part $N_{av}(E)$ related to the mean level density $n_{av}(E) = dN_{av}/dE$, and a fluctuating part which accounts for the difference between $N(E)$ and $N_{av}(E)$. In order to eliminate effects due to variations of the smooth mean level density it is customary to study the fluctuations in the unfolded spectrum

$$\epsilon_i = N_{av}(E_i) , \tag{32}$$

which has a constant mean level density equal to unity. Asymptotically (for large quantum numbers) the smooth part $N_{\mathrm{av}}$ is given by the semiclassical rule, that each quantum state of a $d$-dimensional system occupies a volume $(2\pi\hbar)^d$ of the total phase space $\Gamma$.

Statistical measures frequently used in characterizing level fluctuations are:

(i) The distribution $P(s)$ of spacings $s$ between adjacent levels [nearest neighbour spacing (NNS) distribution]. The probability $P(s)\,\mathrm{d}s$ is the probability for finding a separation of neighbouring levels between $s$ and $s + \mathrm{d}s$.

(ii) The number statistics $n(L)$ of the distribution and the moments associated with it. Given an interval $[\alpha, \alpha + L]$ of length $L$, $n(L)$ counts the number of levels within this spectral range. Averaging over the spectrum yields various moments of the distribution such as the variance $\Sigma_2(L)$, skewness $\gamma_1(L)$ and excess $\gamma_2(L)$.

(iii) Spectral rigidity $\Delta_3(L)$ of the spectrum. Given a substretch $[\alpha, \alpha + L]$ of the spectrum, $\Delta_3(L)$ measures the mean square deviation of the spectral staircase function from the best straight line fit to it

$$\Delta_3(L;\alpha) = \frac{1}{L}\min_{A,B}\int_{\alpha}^{\alpha+L}[N(\epsilon) - A\epsilon - B]^2\,\mathrm{d}\epsilon\,. \tag{33}$$

Note that through the transformation (32) we are dealing with spectra whose average part is the identity, $N_{\mathrm{av}}(\epsilon) = \epsilon$, but for finite segments of the spectrum the best straight line fit may depend slightly on $\alpha$. Averaging over $\alpha$ gives the rigidity $\Delta_3(L)$. $\Delta_3$ is related to the variance $\Sigma_2$ by a non-invertible integral transformation.

The functional forms of the measures listed above are known analytically for some specific model spectra. Two kinds of spectra are particularly important: (a) (Uncorrelated) random level spectra (Poisson spectra), (b) random matrix spectra. In the latter case one distinguishes between ensembles of real symmetric random matrices (Gaussian orthogonal ensemble – GOE) and ensembles of complex Hermitean random matrices (Gaussian unitary ensemble – GUE). The GOE ensemble is the relevant one for the hydrogen atom in a uniform magnetic field, because the Hamiltonians in each $m^{\pi}$ subspace (see eq. 5) are represented by real symmetric matrices. Spectra belonging to the above classes share universal fluctuation properties. Their NNS distributions are given by an exponential

$$P(s) = \mathrm{e}^{-s} \tag{34}$$

for Poisson spectra, and approximately by a Wigner distribution

$$P(s) = \tfrac{1}{2}\pi s\,\mathrm{e}^{-\pi s^2/4} \tag{35}$$

for GOE spectra. Asymptotically (large $L$) the spectral rigidity is given by

$$\Delta_3(L) = L/15 \quad \text{for Poisson spectra} \tag{36}$$

and by

$$\Delta_3(L) \approx (1/\pi^2)\ln L - 0.007 \quad \text{for GOE spectra}\,. \tag{37}$$

Analytic formulae for the moments of the level distributions are more complicated and can be found

e.g. in Bohigas et al. [86]. A graphical presentation of them will be given in the discussion of the results.

The physical motivation for studying level fluctuations accumulates in a conjecture which was first formulated by Bohigas et al. [80], namely that the appearance of universal fluctuation patterns in quantum spectra is linked to the global structure of the underlying classical dynamics: level spectra of classically chaotic systems share random matrix fluctuations, while integrable systems show fluctuations characteristic for random (Poisson) spectra.

In the second half of 1986 three papers [87–89] appeared, in which statistical properties of the energy level spectra of the hydrogen atom in a uniform magnetic field were studied and compared with the predictions of statistical theories. In these earliest papers, the scaled energy was not yet established as the natural parameter governing the classical dynamics, so refs. [88, 89] studied spectra at fixed field strengths, which meant that each spectrum covered a finite range of nonequivalent classical systems. References [87, 88] studied spectra at constant values of the energy divided by the field strength, because this is just the inverse of the effective coupling strength in the quantum mechanical treatment (see section 2.3); constant $E/\gamma$ is actually not far from constant scaled energy, in particular near the zero-field threshold. Independently all three investigations confirmed that the NNS distributions are close to a Poisson distribution for energies where the classical dynamics is regular, and close to a Wigner distribution around the zero-field threshold, where the classical dynamics is chaotic.

More detailed studies [90, 91], now at fixed values of the scaled energy, investigated the transition from the regular (Poisson) to the irregular (GOE) regime. As an example fig. 22 shows various statistical quantities at a scaled energy of $\varepsilon = -0.1$, where the classical dynamics is governed by global chaos. From left to right and top to bottom the figure shows the NNS distribution histogram $P(s)$, the cumulative spacing distribution $\int_0^s P(x)\,\mathrm{d}x$ (which does not depend on the histogram step size), the spectral rigidity $\Delta_3$, the number variance $\Sigma_2$, the skewness $\gamma_1$ and the excess $\gamma_2$; all are shown together with the Poisson and the GOE predictions. The results shown are averages over eight different spectra from various $m^\pi$ subspaces ($m = 0, 1, 2, 3$; $\pi = +, -$), except for the spectral rigidity $\Delta_3$, which was analyzed separately for the two different $z$-parities, because a noticeable parity dependence was observed. Altogether approximately 3000 levels entered the analysis.

There is generally close overall agreement between the results shown in fig. 22 and the predictions of random matrix theories, and this confirms the hypothesis of universal fluctuation patterns in the quantum spectra of classically chaotic systems. However, there are some deviations for large values of $L$, in particular for $\Delta_3$ and $\Sigma_2$. These are related to a breakdown of universality when $L$ becomes larger than some correlation length $L_{\max}$. A semiclassical theory which accounts for these nonuniversal departures has been developed by Berry [92–94] on the basis of Gutzwiller's periodic orbit theory (see section 4.4). It not only gives the same results as the statistical theories for $L \ll L_{\max}$, but also predicts the correct asymptotic behaviour for $L \gg L_{\max}$, where random matrix theories fail.

For the spectral rigidity $\Delta_3$ the semiclassical theory predicts asymptotic saturation. Figure 23 shows the calculated spectral rigidity on a larger scale of $L$-values, again analyzed separately with respect to the $z$-parity. Obviously both curves saturate asymptotically, but they converge to different values corresponding to a parity splitting of 0.040(2). Again this can be understood within the framework of the semiclassical theory. The origin of the parity dependent saturation values are periodic orbits lying on exact symmetry lines of the Hamiltonian. Their influence on the spectrum is different in subspaces belonging to different quantum numbers associated with these discrete symmetries.*) A careful

*) This is worked out quantitatively in section 4.4.

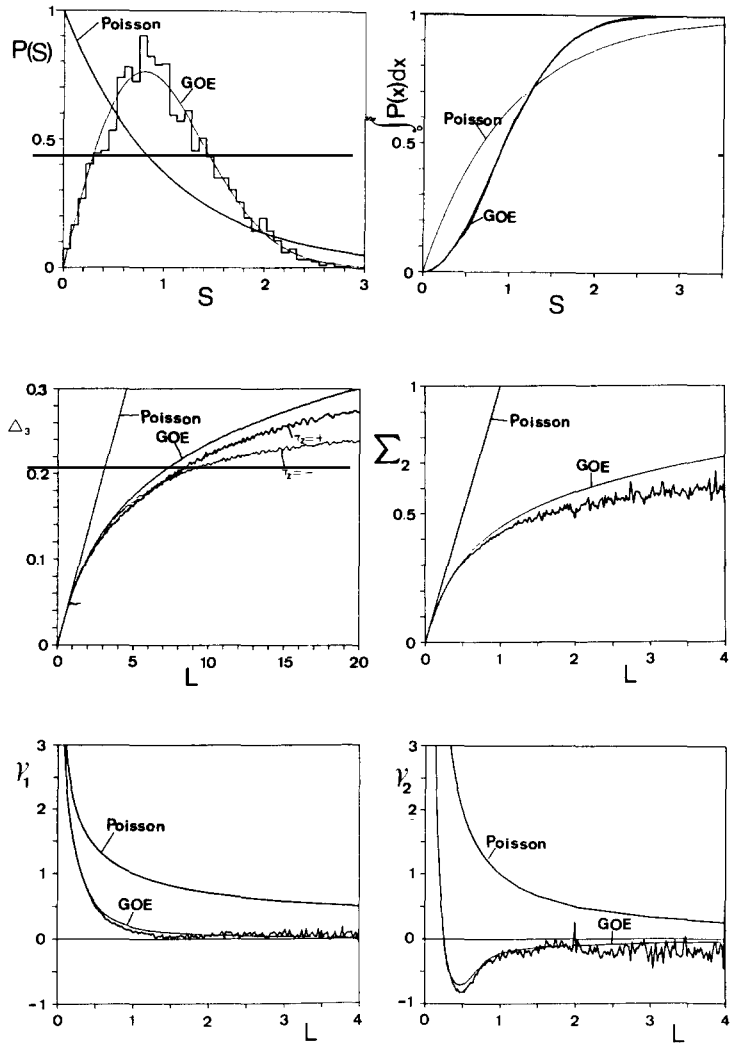


Fig. 22. Statistical properties of the quantum mechanical spectrum at a constant scaled energy $\varepsilon = -0.1$. From left to right and top to bottom the figure shows: the NNS distribution histogram $P(s)$, the cumulative spacing distribution $\int_0^s P(x)\,dx$, the spectral rigidity $\Delta_3$, the number variance $\Sigma_2$, the skewness $\gamma_1$ and the excess $\gamma_2$.

semiclassical analysis [91] gives an asymptotic parity splitting of 0.043, which is quite close to the value observed in fig. 23.

Because of the scaling property of the classical Hamiltonian we can study the statistical properties of the quantum spectra at fixed scaled energy $\varepsilon$ (determining the classical dynamics) and investigate their dependence on $\varepsilon$ as the classical dynamics goes through the transition from regularity to irregularity. Such an analysis is shown in fig. 24 for the NNS distribution histograms. There is a clear transition from a Poisson-like distribution at $\varepsilon = -0.4$ to a Wigner distribution at $\varepsilon = -0.1$. In the transition region the histograms can be approximated fairly well by a Brody distribution [95]

$$P(s) = \alpha(q+1)s^q \, \mathrm{e}^{-\alpha s^{q+1}}, \quad \alpha = [\Gamma((q+2)/(q+1))]^{q+1}, \tag{38}$$

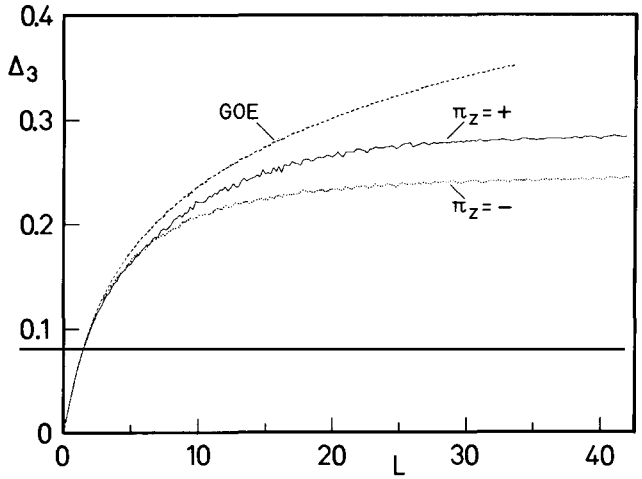


Fig. 23. Spectral rigidity (33) at $\varepsilon = -0.1$ as a function of $L$.

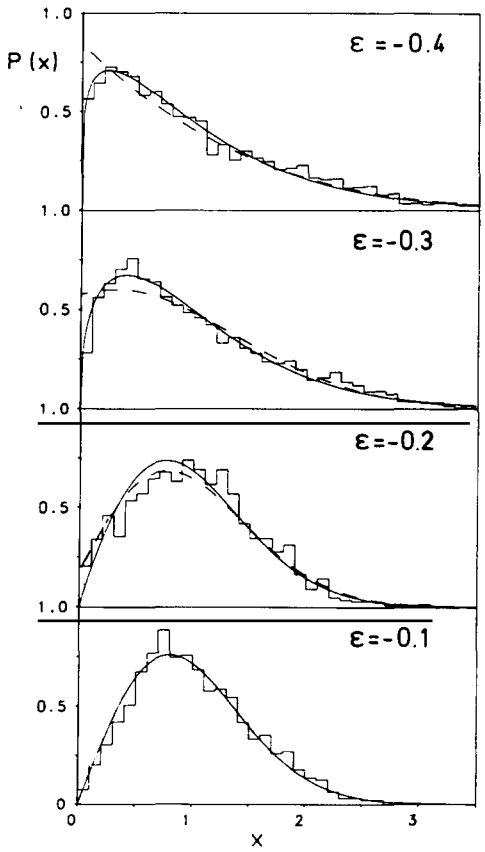


Fig. 24. NNS distributions $P(x)$ for scaled energies $\varepsilon$ varying from $-0.4$ to $-0.1$. The solid lines show attempts to fit the histograms with Brody's formula (38), the dashed lines represent the interpolation formula of Berry and Robnik [96]. (From ref. [90].)

which interpolates between the regular Poisson distribution ($q = 0$) and the irregular Wigner distribution ($q = 1$) and is represented by the solid lines in fig. 24. Also shown in the figure are attempts to fit the histograms with a distribution proposed by Berry and Robnik [96] (dashed lines), which is obtained by the independent superposition of a spectrum obeying Poisson statistics with weight $q$ and a spectrum obeying Wigner statistics with weight $1 - q$. Although the idea behind the Berry–Robnik distribution seems very reasonable, the fits were generally poor compared to fits obtained with the Brody distribution. One reason for the poor performance of the Berry–Robnik distribution in the present case is, that the levels belonging to the regular part of the spectrum do not obey a Poisson distribution, but behave more like the levels of a two-dimensional harmonic oscillator [91].

More detailed investigations reveal that the transition from Poisson to Wigner statistics in the NNS distributions is not as smooth as might be expected from fig. 24. It seems to be difficult if not impossible to find a quantitative description of the NNS distributions in the transition regime between regularity and irregularity. The reason for this is that the spectral statistics can depend sensitively on nonuniversal, system-specific details of the underlying classical dynamics [91]. This can be seen more clearly in other statistical measures shown in figs. 25 and 26.

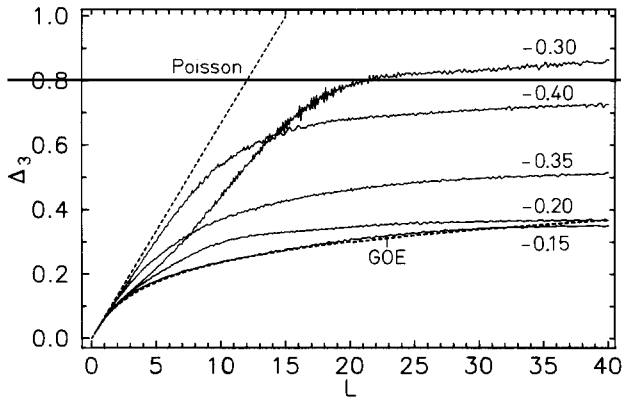


Fig. 25. Spectral rigidity $\Delta_3$ as function of $L$ for various values of the scaled energy $\varepsilon$. (From ref. [91].)

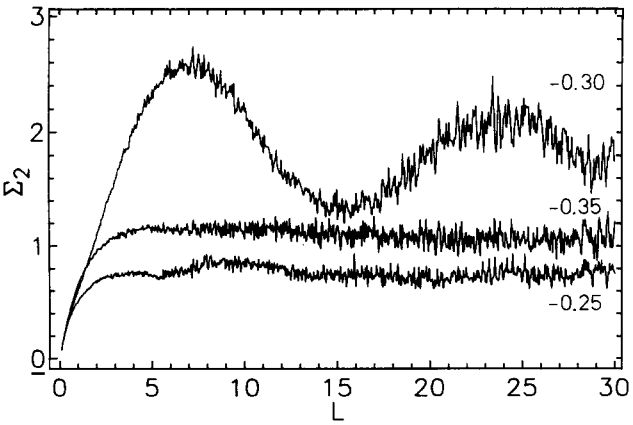


Fig. 26. Number variance $\Sigma_2$ as function of $L$ for three values of the scaled energy $\varepsilon$. (From ref. [91].)

Figure 25 shows the spectral rigidity $\Delta_3$ for various values of the scaled energy $\varepsilon$, together with the predictions of the Poisson and the GOE cases. In the nonsaturated region $L < 5$ one clearly sees the transition from Poisson to random matrix statistics as $\varepsilon$ is increased from $-0.4$ to $-0.15$. However, for larger values of $L$, the spectral rigidity at $\varepsilon = -0.3$ does not conform to the general trend and saturates at a much larger value than that observed for the other values of $\varepsilon$. An even more dramatic deviation from the general trend is observed for the number variance $\Sigma_2$ shown in fig. 26. At $\varepsilon = -0.3$ the number variance $\Sigma_2(L)$ might be expected to be a smoothly varying curve lying between the corresponding curves for $\varepsilon = -0.25$ and $\varepsilon = -0.35$; however it is a strongly oscillating curve which lies well above the other two curves for $L > 3$.

These deviations of various statistical measures from a smooth $\varepsilon$-dependence near $\varepsilon = -0.3$ can be readily explained within the framework of Berry's semiclassical theory as a consequence of the properties of certain stable periodic orbits [91]. The extraordinary features observed at $\varepsilon = -0.3$ can be traced to the stable periodic orbit perpendicular to the field ($\mathrm{I}_1$), which accidentally has a low rational winding number at this value of $\varepsilon$. This causes many systematic near-degeneracies in the regular part of the spectrum (see section 4.4), which naturally has a strong influence on the number statistics.

The statistical analysis in this chapter applied to the fluctuating part in the density of states. Other physical quantities can also be considered. Recently Wunner et al. [141] studied transition strength fluctuations (distribution of oscillator strength) and again found good agreement with random matrix predictions. The same is to be expected for the decay widths of resonant states above the ionization limit. Random matrix theories predict very narrow decay widths as the most probable ones. A quantum mechanical mechanism to obtain such long-living states was given by Friedrich and Wintgen [46]. Recent experiments seem to confirm the existence of these narrow states [142].

To summarize, the statistical measures studied in this section follow the universal predictions of statistical theories quite well, as long as the level fluctuations are analyzed on a small scale. Agreement is good for local properties of the level fluctuations. On larger scales however (global properties), nonuniversal features reflecting special properties of the underlying classical dynamics, become dominant and may lead to extraordinary behaviour of the statistical measures. It turns out that the knowledge of the classical periodic orbits is useful and necessary to understand the complex spectra. The influence of periodic classical orbits on the properties of quantum spectra is discussed quantitatively in the next two sections.

### *4.3. History of the quasi-Landau phenomenon*

The discovery of almost equidistant peaks in the photoabsorption spectra of atoms in a magnetic field [56] played a major role in generating the widespread attention given to the problem of atoms in magnetic fields in recent years. Near the ionization threshold the separation of the peaks is roughly 1.5 times the cyclotron energy $\hbar\omega_c = 2\hbar\omega$, which corresponds to the separation of the Landau states of free electrons in a magnetic field, hence the name quasi-Landau oscillations.

Solutions of the one-dimensional Schrödinger equation for an electron moving in the plane perpendicular to the magnetic field actually give energy levels with a spacing of roughly 1.5 times $\hbar\omega_c$, as was soon found out on the basis of semiclassical (WKB) investigations [97–99]. The early success of this simple explanation of the spacing of the quasi-Landau peaks led to the widespread view that these peaks were due to resonant photoabsorption into individual quantum states in which the motion of the electron is localized in the plane perpendicular to the direction of the magnetic field [18, 57, 98–102]. This picture was also consistent with absence of quasi-Landau peaks for transitions into $m^{\pi}$ subspaces

with negative $z$-parity, because the negative parity wave functions all vanish in the plane perpendicular to the field. It was shown later [67, 103], that the disappearance of quasi-Landau structure in subspaces with negative $z$-parity is a property of the transition operator involved and not of the final state density.

First ab initio quantum calculations of states at the zero-field threshold $E = 0$ and at field strengths somewhat higher than laboratory field strengths showed that the above picture of a quasi-Landau peak as due to a single quantum state with a dominant oscillator strength is at best a severe over-simplification [104]. The quasi-Landau region is highly irregular, and it is in general not possible to arrange the spectrum in simple sequences of bound (or resonant) states. On the other hand, the experimental data on the quasi-Landau "resonances" showed smoothly modulated cross sections and did not necessarily imply an identification of the modulation peaks with individual quantum states. The experimentally observed quasi-Landau oscillations can in fact be related to the (classical) motion of the electron in the plane perpendicular to the field without invoking the existence of prominent individual quantum states at the peak positions, as is described below.

One way of correlating modulations in the cross sections with closed classical orbits is the picture of a wave packet recurring to its starting point after each traversal of the closed orbit. The modulation peaks are due to constructive interference on recurrence, and this occurs when the "resonance condition"

$$S(E) = \frac{1}{2\pi\hbar} \oint \boldsymbol{p}\, \mathrm{d}\boldsymbol{r} = n \tag{39}$$

is fulfilled [105–108]. This resonance condition is not a quantization condition defining the energies of individual quantum states, but it can determine the positions of modulation peaks in cross sections or spectral densities. This general picture is not only applicable to the quasi-Landau modulations of atoms in a magnetic field, but also to a variety of other physical systems showing similarly modulated spectra, e.g. atoms in external electric fields [109, 110, 126, 143], negatively charged ions in external fields [111–114], the spectra of the $H_3^+$ [115] and the $H_2O$ molecules [134].

The interest in the quasi-Landau phenomenon received a boost after 1986, when Welge and collaborators studying photoabsorption spectra of atomic hydrogen reported a new series of more closely lying peaks for transitions into $m^{\pi}$ subspaces with negative $z$-parity [7]. These peaks could be related via the resonance condition (39) to the first orbit $I_2$ of the series of non-straight-line periodic orbits shown in fig. 19. Fourier transforming the measured cross sections soon revealed a whole series of modulation frequencies, and these were correlated with the other orbits of the series [8].

### *4.4. Gutzwiller's trace formula*

A quantitative description of how periodic classical orbits influence quantum mechanical observables is provided by a theory developed by Gutzwiller [79, 116–118], Balian and Bloch [119] and Berry and coworkers [120–122]. This theory is a semiclassical approximation of Feynman's path integral formalism [123]. The quantum mechanical spectral density

$$n(E) = \sum_i \delta(E - E_i) \tag{40}$$

is written as the sum of a smooth part $n_{\mathrm{av}}(E)$, the mean level density, and a fluctuating part. The

fluctuating part is given explicitly as a sum over the periodic orbits of the classical system:

$$n(E) - n_{\mathrm{av}}(E) = -\mathrm{Im} \sum_{r,j} a_{rj} \exp\{2\pi \mathrm{i} j[S_r(E) - \mu_r]\} . \tag{41}$$

The label $r$ runs over all primitive orbits and the label $j = 1, 2, 3, \ldots$ counts the number of traversals of the periodic orbit; $\mu_r$ is an appropriate Morse index for the phase, which is analogous to the Maslov index familiar in semiclassical quantization and depends on the focussing of trajectories close to the periodic orbit [122].

The beauty of eq. (41) is that it applies irrespective of whether the system is regular and the orbits stable, or whether the system is chaotic and the orbits unstable. The information about the stability of an orbit is contained in the amplitude factors $a_{rj}$. For a stable periodic orbit these factors oscillate or behave as a power in $j$, depending on whether the orbit is isolated in phase space or is embedded on a (resonant) torus [120–122]. For unstable periodic orbits the amplitude factors $a_{rj}$ decay exponentially with $j$ (see below). The contribution of a primitive periodic orbit $r$ together with all its repetitions to the density of states is thus a more or less pronounced peak when $S_r - \mu_r$ is a whole number. Except for the modification due to the Morse index, this is precisely the resonance condition (39). However, the contribution of a single periodic orbit in the trace formula (41) does not lead to singularities (individual quantum states) in the density of states.*)

Formulae of the type (41) apply not only to the energy level density but also to other quantum mechanical observables such as the photoabsorption cross sections from a low-lying state [124–126] or expectation values of operators having a classical counterpart [127].

The resonance condition (39) (ignoring for simplicity the Morse index) can be expressed in terms of the scaled coordinates and momenta (20)

$$\tilde{S}(\varepsilon) = \frac{1}{2\pi\hbar} \oint \tilde{\boldsymbol{p}} \, \mathrm{d}\tilde{\boldsymbol{r}} = \gamma^{1/3} \frac{1}{2\pi\hbar} \oint \boldsymbol{p} \, \mathrm{d}\boldsymbol{r} = \gamma^{1/3} n ; \tag{42}$$

$\tilde{S}(\varepsilon)$ is the *scaled action* and depends only on the scaled energy which determines the classical dynamics. The scaled resonance condition (42) means that the modulations related to a given periodic orbit $r$ are, at fixed values of the scaled energy $\varepsilon$, located at

$$\gamma^{-1/3} = \sqrt{\varepsilon/E} = n/\tilde{S}_r(\varepsilon) , \tag{43}$$

i.e. they are equidistant on a scale linear in $\gamma^{-1/3}$. Equation (43) shows that a comparison of classical and quantum mechanics is most appropriately done by studying spectra at fixed values of the scaled energy $\varepsilon$ and as functions of $\gamma^{-1/3}$. Modulation peaks associated with a given periodic orbit $r$ are then equidistant and separated by the inverse scaled action $1/\tilde{S}_r(\varepsilon)$. In the Fourier-transformed spectra depending on a conjugate variable, which we call $\gamma^{1/3}$ for simplicity, such regular modulations appear as prominent peaks situated at

$$\gamma^{1/3} = \tilde{S}(\varepsilon) . \tag{44}$$

*) Note however, that using the trace formula (41) as direct quantization formula for stable *and* isolated orbits can approximate the regular part of the spectrum very accurately!

In contrast, studying quantum spectra as functions of the (non-scaled) energy $E$ at fixed field strengths $\gamma$ involves averaging over a range of scaled energies determining the classical dynamics, and Fourier transforming such spectra leads to broadened peaks in the time domain, the locations of the peaks being given by the periods of the orbits. These peaks may be washed out, however, because the periods of the orbits depend on the energy.

Power spectra (i.e. squared Fourier amplitudes) of the fluctuating part of the energy level density are shown in fig. 27 for various $m^{\pi}$ subspaces at the scaled energy $\varepsilon = -0.2$. The power spectra do indeed show several sharp peaks which can be correlated with classical orbits. A remarkable feature in fig. 27 is that the power spectra in the different $m^{\pi}$ subspaces are almost identical, although the details of the underlying spectra are of course quite different. The reason for the similarity of the power spectra is, that the scaled azimuthal quantum number $\tilde{m} = \gamma^{1/3} m$ becomes negligibly small in the dense part of the spectrum (small field strengths) so that the classical dynamics becomes independent of $m$. (Note however, that the peak at $\tilde{S} = 1.58$ is strong for $m = 0$, less pronounced for $m = 1$ and almost absent in the $m = 2$ subspaces. This point will be discussed later in this section.)

For a more quantitative analysis it is useful to recall the derivation of the trace formula (41). The density of states can be expressed as the trace of the Green's function

$$n(E) = -\mathrm{Im}[(1/\pi)\,\mathrm{Tr}\,G(E)]\,. \tag{45}$$

The Green's function is the Laplace transform of the time evolution propagator $K$,

$$G(E) = -\frac{\mathrm{i}}{\hbar}\int_0^{\infty} \mathrm{e}^{(\mathrm{i}/\hbar)Et} K(t)\,\mathrm{d}t\,, \tag{46}$$

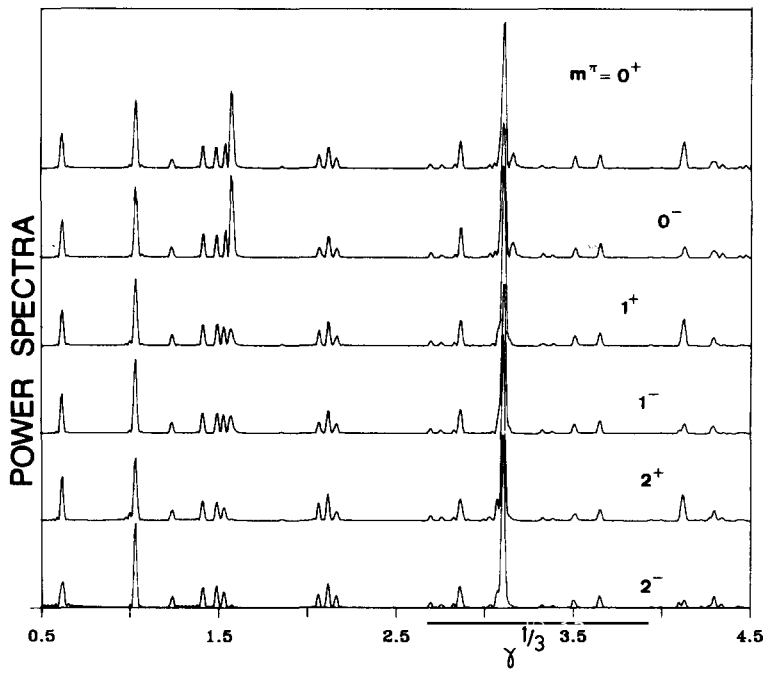


Fig. 27. Squared Fourier transforms of the fluctuating part of the cumulative level density in various $m^{\pi}$ subspaces.

$$K(t) = \mathrm{e}^{-(\mathrm{i}/\hbar)Ht} . \tag{47}$$

In Feynman's formulation of quantum mechanics [123] the propagator is expressed as a path integral,

$$K(\boldsymbol{q}', \boldsymbol{q}'', t) = \int_{\boldsymbol{q}'}^{\boldsymbol{q}''} \mathscr{D}[\boldsymbol{q}]\, \mathrm{e}^{(\mathrm{i}/\hbar)W[\boldsymbol{q}]} , \tag{48}$$

where $W = \int_0^t L(\boldsymbol{q}, \dot{\boldsymbol{q}})\, \mathrm{d}t$ is the action written as the time integral over the Lagrangian. The semiclassical approximation consists in evaluating the integrals by the method of stationary phase, which yields significant contributions to the density of states from the classical periodic orbits only. These orbits contribute sinusoidal corrections to the mean level density $n_{\mathrm{av}}$, which is given by the size of the energy shell in phase space

$$n(E) = n_{\mathrm{av}}(E) - \mathrm{Im} \sum_r \frac{\mathrm{i}T_r}{\pi\hbar} \sum_{j=1}^{\infty} \frac{\exp[\mathrm{i}j(S_r/\hbar - \mu_r \pi/2)]}{[\det(\boldsymbol{M}_r^j - 1)]^{1/2}} . \tag{49}$$

Equation (49) is the so-called trace formula in which the sums run over all primitive periodic orbits $r$ with periods $T_r$ and actions $S_r$ and over all repetitions $j$ of the primitive orbits. $\mu_r$ is the respective Morse index and $\boldsymbol{M}_r$ is the $2 \times 2$ stability matrix describing the time evolution of transverse displacements off the periodic orbit.*) The eigenvalues of $\boldsymbol{M}_r$ define the type of fixed point of the periodic orbit in the Poincaré surface of section. The determinant is given, depending on the type of fixed point, by

$$\begin{aligned} \det(\boldsymbol{M}^j - 1) &= 4 \sinh^2(j\Lambda/2) , && \text{hyperbolic} , \\ &= -4 \cosh^2(j\Lambda/2) , && \text{inverse hyperbolic} , \\ &= -4 \sin^2(j\pi\nu_{\mathrm{w}}) , && \text{elliptical} , \end{aligned} \tag{50}$$

$\Lambda = \lambda T$ is the Liapunov exponent of an unstable orbit in the Poincaré map, and $\nu_{\mathrm{w}}$ is the winding number of a stable orbit (see section 3.4).

Two modifications are necessary if the Hamiltonian has discrete symmetries and if we are studying spectra in subspaces of eigenfunctions of these symmetries. Firstly, the Green's function has to be adapted to the symmetries before taking the trace in eq. (45). As a consequence, periodic orbits can contribute e.g. with half-integer traversals (corresponding to $j = 1/2,\ 3/2,\ 5/2, \ldots$), if the orbits are invariant under these symmetry transformations.**) Secondly, periodic orbits which are selfretracing along symmetry lines contribute differently to different discrete subspaces. This can be seen by expanding the amplitudes of e.g. an unstable orbit, eq. (50)

$$\frac{1}{2\sinh(j\Lambda/2)} = \sum_{k=0}^{\infty} \mathrm{e}^{-(k+1/2)j\Lambda} . \tag{51}$$

Equation (51) gives the decomposition of the amplitude in (50) into the various harmonic excitations

*) $\boldsymbol{M}_r$ is obtained from the full $4 \times 4$ monodromy matrix (29) by an orthogonal transformation [116].

**) Generally, if the underlying potential has a $C_{nv}$-symmetry then symmetry-invariant periodic orbits can contribute with the $n$th part of their total length. In our case $n = 2$, see eq. (1).

$k$ perpendicular to the orbit. $(-1)^k$ defines the "local" parity of the transversal excitations. If this local parity coincides with an exact discrete symmetry of the Hamiltonian, viz. the symmetry orbits itself, then the amplitude (51) has to be split into its odd and even parts by resumming over odd and even values of $k$ separately. In the present system, the straight line orbits perpendicular and parallel to the field ($I_1$ and $I_\infty$) are such selfretracing orbits along symmetry lines. The latter modification is the reason why the peak at $\tilde{S} = 1.58$ in fig. 27 becomes less pronounced with increasing azimuthal quantum number $m$.*) This peak is correlated to the periodic orbit $I_\infty$ parallel to the field, which is unstable at $\varepsilon = -0.2$. Since the scaled azimuthal quantum number $\tilde{m} = \gamma^{1/3} m$ tends to zero for high excitations, the classical dynamics is quite generally independent of $m$. The main effect of the azimuthal quantum number is its influence on the behaviour of the wave functions near $\tilde{\rho} = 0$, which is given by $\psi \propto \rho^{|m|}$. Thus one has to sum over odd or even $k \geq m$ in eq. (51). The corresponding amplitudes then differ by a factor

$$a_{I_\infty j}^{(m)} = (-1)^m \, e^{-mj\Lambda} a_{I_\infty j}^{(m=0)} . \tag{52}$$

The minus sign applies because the fixed point is inverse hyperbolic. Thus the peak belonging to the orbit parallel to the field becomes exponentially damped with increasing $m$.

The same decomposition of the amplitude has to be performed for the periodic orbit $I_1$ perpendicular to the field. However, at $\varepsilon = -0.2$ this does not affect the heights of the related peaks in the power spectrum, because the orbit is stable at this scaled energy. Expanding the sine in eq. (50) yields amplitudes which differ only in phase

$$a_{I_1 j}^{-} / a_{I_1 j}^{+} = e^{-2\pi i j \nu_w} . \tag{53}$$

Thus the peaks in the power spectrum are of the same magnitude for the orbit $I_1$, in agreement with fig. 27. This is different of course when the orbit becomes unstable, e.g. at $\varepsilon = -0.1$, where $I_1$ corresponds to an inverse hyperbolic fixed point in the surface of section and the Liapunov exponent of the Poincaré map is $\Lambda = 0.6080$. Thus eq. (51) predicts modulations with amplitudes differing by $a_{I_1 j}^{-} / a_{I_1 j}^{+} = -0.544$; the value found by Fourier-transforming the spectra belonging to different $z$-parities is in fact $-0.54$. This connection between the quantum mechanical spectrum and the properties of the classical orbits means that we can determine the Liapunov exponent of the periodic orbit (with an accuracy of 1%) and the type of fixed point in the Poincaré surface of section by solving the linear Schrödinger equation without having to follow the nonlinear evolution of the classical dynamics.

The effect of symmetrization of the Green's function on the spectra can be illustrated by contrasting the power spectra shown in fig. 27 with power spectra derived from parity-mixed level sequences as shown in fig. 28. Although the orbit $I_1$ perpendicular to the field has the shortest scaled action, $\tilde{S}_{I_1}(\varepsilon = -0.2) = 1.033\,05$, of all periodic orbits, the power spectra in fig. 27 show a sharp peak at the smaller value $\gamma^{1/3} = 0.62$ in each $m^\pi$ subspace. This value corresponds to the scaled action for half a traversal of the almost circular orbit (C) (the numerical value is $\frac{1}{2}\tilde{S}_C = 0.617\,30$), which is symmetric under a coordinate rotation through the angle $\pi$. This peak vanishes exactly in the Fourier transform of the parity-mixed spectrum containing all levels of the $m^\pi = 0^+$ and the $m^\pi = 0^-$ subspaces together (fig. 28). In fig. 28, the almost circular orbit manifests itself only at scaled actions $\tilde{S}_C = 1.234\,60$, $2\tilde{S}_C = 2.469\,20, \ldots$ corresponding to full traversals of the orbit.

The peaks in fig. 27 can be fully accounted for by the trace formula. Each peak can be associated

*) This modification also causes the observed parity dependences of the statistical measures discussed in section 4.2.

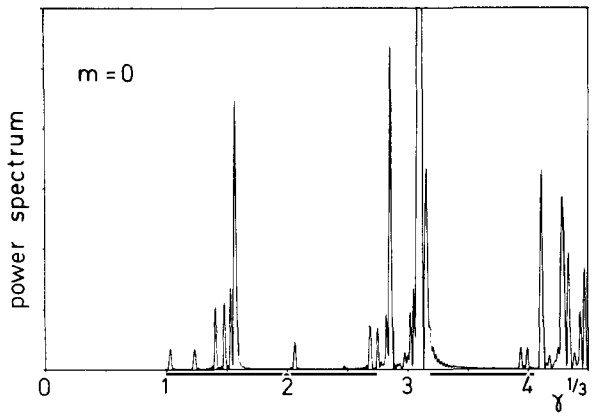


Fig. 28. Squared Fourier transform of the fluctuating part of the energy level density for the spectrum consisting of all levels of the $m^{\pi} = 0^{+}$ and $m^{\pi} = 0^{-}$ subspaces together.

with a classical periodic orbit, and for each periodic orbit (with a scaled action in the range covered by the abscissa) there is a corresponding peak in the Fourier transformed spectra. The locations of the peaks agree with the directly calculated scaled actions of the classical orbits typically to within a few parts in $10^4$. (For further details see ref. [128].) Thus the semiclassical trace formula provides a simple, elegant and powerful way of quantitatively explaining the quantum spectra in the low frequency domain.

Having established the idea that quantum spectra can be decomposed into oscillating contributions associated with classical periodic orbits, one might try to use the classical orbits to calculate the quantum level density. In order to obtain the full semiclassical spectrum one would have to sum over all periodic orbits including arbitrarily long periods or rather large scaled actions. To do this numerically is a hopeless task. In order to obtain a complete knowledge of the periodic orbits one needs to know the symbolic organization of the periodic orbits [129] or at least an algorithm to find all of them. Until very recently such coding schemes existed only for some Hamiltonian systems without bifurcations [74, 130, 135]; the symbolic organization of the periodic orbits for the hydrogen atom in a uniform magnetic field has been worked out in ref. [136]. However even in the limit of including all periodic orbits in the trace formula, it is not clear whether the sum would really reproduce all the delta-function spikes associated with the true quantum levels [122, 137]. The reason for this is that the trace formula is certainly not absolutely convergent. Presumably it is not convergent at all so that it can be used as an asymptotic sum only [138]. Incorporating the symbolic organization of the periodic orbits together with refined summation techniques may however give the analytic continuation of the trace formula. This is indicated by some recent work in refs. [129, 139].

The complications of a summation over all periodic orbits can be avoided if we include only the simplest orbits in an attempt to generate a finite resolution density of states, the resolution being determined by the longest period (the largest scaled action) amongst the orbits included. Figure 29a shows the minimal version of such a calculation [131]. Only the two simplest periodic orbits, $I_1$ and C, are included and their contributions from up to one full traversal yield the thin solid line. The smoothed fluctuating part of the exact quantum mechanical spectrum is shown as the thick solid line (for more details see ref. [131]). Figure 29a shows that this minimal calculation based on only two classical periodic orbits is able to reproduce the gross structure of the quantum spectrum with remarkable

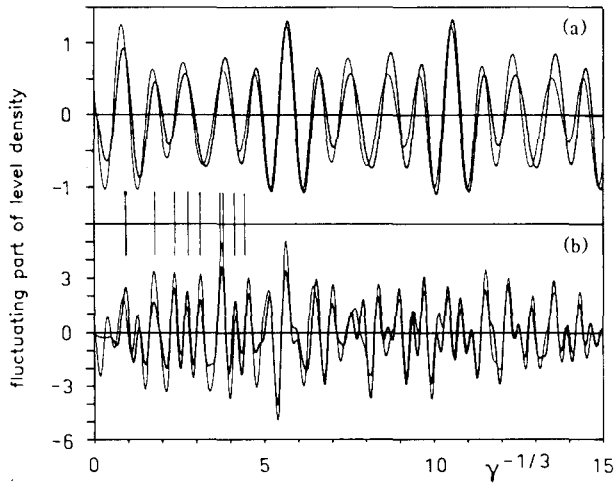


Fig. 29. Finite resolution spectra (thin solid lines) obtained on the basis of (a) the two shortest periodic orbits and (b) including periodic orbits with scaled actions up to three. The vertical lines in the centre of the figure show the energies of the first few quantum states (from ref. [131]).

accuracy. Figure 29b shows the results of a more involved calculation where the sum in the trace formula includes all periodic orbits with scaled actions less than $\tilde{S}_{max} = 3$. This results in nineteen contributions from thirteen primitive orbits. Again close agreement with the smoothed quantum spectrum is observed, now on a finer scale.

Figure 29 demonstrates that the trace formula is able to reproduce a finite-resolution density of states. In spectral regions where the resolution becomes finer than the mean separation of states, the peaks appearing in the level density are due to individual resolved quantum states. This is the case for $\gamma^{-1/3} < 4.5$ in the figure. The exact quantum eigenvalues agree with the peak positions to within a few per cent of the mean level spacing, even down to the ground state. This is somewhat surprising, because one does not necessarily expect semiclassical theories to be accurate near the ground state [131]. In addition, excited levels up to the ninth eigenvalue are predicted quite accurately by the simple sum including only thirteen classical orbits.

Periodic orbit analyses of quantum spectra have been performed not only for the density of states, but also for calculated [67, 107, 108, 126] and measured [7, 8, 132, 133] photoabsorption cross sections. These cross sections depend on dipole transition matrix elements involving an initial wavefunction which, compared to the wavefunctions of the highly excited final states, are confined to a region very close to the origin (i.e. the nucleus). In the appropriate semiclassical treatment only such classical orbits are important which start at the origin. Recall that, because of the Coulombic nature of the potential at the origin, all orbits which recur to the origin retrace their path and are hence periodic. A complete listing of all periodic orbits passing through the origin and with scaled actions up to $\tilde{S} = 4$ at the zero-field threshold $\varepsilon = 0$ is given in ref. [67].

Gutzwiller's trace formula for the fluctuating part of the level density, and corresponding formulae for (the fluctuating part of) other observables such as photoabsorption cross sections, establish a connection between periodic classical orbits and quantum mechanical spectra. In particular, isolated periodic orbits with short periods or small (scaled) actions lead to peaks in the quantum mechanical spectra, and the positions of the peaks are determined by a resonance condition resembling a semiclassical quantization condition. The observed correlation between so-called "quasi-Landau reso-

nances" and classical periodic orbits thus has a sound theoretical foundation which reaches deeper than early interpretations based on one-dimensional WKB calculations.

To arrive at a semiclassical understanding of "chaotic" wavefunctions is a much harder task (see e.g. refs. [144, 145]). A theory based on Gutzwiller's idea has been developed recently by Bogomolny [146]. Investigations currently in progress for the hydrogen atom in a magnetic field again indicate that the periodic orbits play an essential role in understanding the complex structure of the wavefunctions [141, 147, 148].

## 5. Summary

The hydrogen atom in a uniform magnetic field is a uniquely simple example of a real physical system showing all the features currently causing excitement in the field of small dynamical systems exhibiting classically chaotic dynamics.

The quantum mechanical Schrödinger equation has been solved numerically with high accuracy for arbitrary field strengths and energies very close to or up to (depending on field strength) the zero-field threshold. Within the accuracy of experimental measurements, the calculated spectra reproduce spectra observed in photoabsorption experiments, and this connection to a real laboratory system gives added weight to all conclusions drawn from a theoretical or numerical analysis.

In the plane spanned by the energy $E$ and the field strength $\gamma$ there is a perturbative regime of low field strengths and excitation energies, where the quantum mechanical levels in each $m^{\pi}$ subspace can be labelled by the quantum number $n$ of the manifold of unperturbed (i.e. field-free) hydrogenic states from which they evolve, and an intra-shell label $k$ counting the states in each manifold. In this region the Hamiltonian is approximately separable and the label $k$ is associated with an additional approximate integral of the motion. The region of approximate separability actually extends well into the $n$-mixing regime, where various $n$-manifolds overlap. Approximate separability breaks down as we approach the zero-field threshold at $E = 0$, regardless of field strength. At very high field strengths, where the energy of a Landau excitation perpendicular to the direction of the magnetic field becomes comparable to or larger than the Rydberg energy, the system becomes simpler again and can be accurately described by an expansion in coupled Landau channels.

The classical dynamics of the hydrogen atom in a uniform magnetic field does not depend on energy $E$ and field strength $\gamma$ separately but is determined, to within a trivial similarity transformation, solely by the scaled energy $\varepsilon = E/\gamma^{2/3}$. Near the field free limit $\varepsilon \to -\infty$ the classical motion is regular and confined to invariant tori. Around $\varepsilon \approx -0.35$ there is a comparatively sudden transition to irregular (chaotic) motion, with the last elliptical islands of regularity disappearing at $\varepsilon = -0.127\,268\,612$. Increasing chaoticity is expressed in an increasing fraction of irregular orbits in phase space and also in increasing Liapunov exponents and increasing numbers of periodic orbits.

The classical transition to chaos is accompanied by corresponding transitions in statistical properties of the quantum spectra. Fine scale quantities such as nearest neighbour spacings show the expected transition from the expectations associated with random level spectra in the classically regular region to spectra associated with random matrix ensembles in the classically chaotic region. For statistical quantities depending on correlations of somewhat longer range in the spectra, these transitions are however not at all uniform and show a sensitive dependence on system specific non-universal properties such as the occurrence of prominent simple periodic classical orbits.

A knowledge of the periodic classical orbits of the system is important for understanding the general

structure of the quantum level spectra and of other observable quantities such as photoabsorption spectra. The connection between quantum spectra and periodic classical orbits is quantitatively expressed in Gutzwiller's trace formula. Finite resolution spectra can already be described quite accurately using the knowledge of only a small number (two) of simple periodic orbits with short periods or small actions. We now understand, that the modulation peaks in photoabsorption spectra, which have long been known under the name "quasi-Landau resonances" are, together with the multitude of more recently discovered further modulations, simply a manifestation of the occurrence of prominent unstable periodic orbits in the classically chaotic region.

## Acknowledgements

It is a pleasure to thank numerous colleagues who have helped us in discussions and collaborations in recent years. We have particularly profited from contacts with G. Alber, E.B. Bogomolny, O. Bohigas, J.S. Briggs, J.T. Broad, D. Delande, B. Eckhardt, J.C. Gay, M.C. Gutzwiller, A. Holle, A. Hönig, J. Main, H. Marxer, R. Niemeier, K. Richter, P. Richter, H. Ruder, W. Schweizer, K.T. Taylor, H.-A. Weidenmüller, G. Wunner, and G. Zeller. We thank the Deutsche Forschungsgemeinschaft for substantial financial support during the last years. This work was also supported by the NSF under Grant No. PHY82-17853, supplemented by funds from NASA.

## References

[1] Y. Sinai, Russ. Math. Surv. 25 (1970) 137.
[2] L.A. Buminovich, Funct. Anal. Appl. 8 (1974) 254; Commun. Math. Phys. 65 (1979) 295.
[3] G. Benettin, Physica D 13 (1984) 211.
[4] M. Henon and C. Heiles, Astron. J. 69 (1964) 73.
[5] R.A. Pullen and A.R. Edmonds, J. Phys. A 14 (1981) L477.
[6] E. Haller, H. Köppel and L.S. Cederbaum, Phys. Rev. Lett. 52 (1984) 1655;
H.-D. Meyer, E. Haller, H. Köppel and L.S. Cederbaum, J. Phys. A 17 (1984) L831.
[7] A. Holle, G. Wiebusch, J. Main, B. Hager, H. Rottke and K.H. Welge, Phys. Rev. Lett. 56 (1986) 2594.
[8] J. Main, G. Wiebusch, A. Holle and K.H. Welge, Phys. Rev. Lett. 57 (1986) 2789.
[9] K.A.U. Lindgren and J. Virtamo, J. Phys. B 12 (1979) 3465;
B.G.S. Doman, J. Phys. B 13 (1980) 3335.
[10] R.H. Garstang, Rep. Prog. Phys. 40 (1977) 105.
[11] J.E. Avron, I.W. Herbst and B. Simon, Ann. Phys. (NY) 114 (1979) 431.
[12] V.B. Pavlov-Verevkin and B.I. Zhilinskii, Phys. Lett. A 78 (1980) 244.
[13] G. Wunner, H. Ruder and H. Herold, Z. Phys. A 79 (1980) 159; Astrophys. J. 247 (1981) 374;
H. Herold, H. Ruder and G. Wunner, J. Phys. B 14 (1981) 751.
[14] M. Vincke and D. Baye, J. Phys. B 21 (1988) 2407.
[15] H.C. Praddaude, Phys. Rev. A 6 (1972) 1321.
[16] E.R. Smith, R.J.W. Henry, G.L. Surmelian, R.F. O'Connell and A.K. Rajagopal, Phys. Rev. D 6 (1972) 3700.
[17] J. Simola and J. Virtamo, J. Phys. B 11 (1978) 3309.
[18] C.W. Clark and K.T. Taylor, J. Phys. B 13 (1980) L737; 15 (1982) 1175.
[19] J.E. Bayfield, Phys. Rep. 51 (1979) 317.
[20] D. Kleppner, M.G. Littman and M.L. Zimmerman, in: Rydberg States of Atoms and Molecules, eds R.F. Stebbings and F.B. Dunning (Cambridge Univ. Press, Cambridge, 1983) p. 73.
[21] J.C. Gay, in: Progress in Atomic Spectroscopy Part C, eds H.J. Beyer and H. Kleinpoppen (Plenum, New York, 1984) p. 177.
[22] C.W. Clark, K.T. Lu and A.F. Starace, in: Progress in Atomic Spectroscopy Part C, eds H.J. Beyer and H. Kleinpoppen (Plenum, New York, 1984) p. 247.

[23] D. Delande, F. Biraben and J.C. Gay, in: New Trends in Atomic Physics, Les Houches Session XXXVIII (Elsevier, Amsterdam, 1984) p. 351.
[24] C.W. Clark, in: Atomic Excitation and Recombination in External Fields, eds M.H. Nayfeh and C.W. Clark (Gordon and Breach, London, 1985) p. 17.
[25] J.C. Guillou and J. Zinn-Justin, Ann. Phys. (NY) 147 (1983) 57.
[26] W. Rösner, G. Wunner, H. Herold and H. Ruder, J. Phys. B 17 (1984) 29.
[27] P.C. Rech, M.R. Gallas and J.A.C. Gallas, J. Phys. B 19 (1987) L215.
[28] B.H. Cho, N.N. Choi and G.O. Kim, J. Phys. B 20 (1987) L453.
[29] C.R. Liu and A.F. Starace, Phys. Rev. A 35 (1987) 647.
[30] D. Delande and J.C. Gay, J. Phys. B 19 (1986) L173.
[31] D. Wintgen, Doctoral Thesis, Technical University Munich (1985) unpublished.
[32] T.P. Grozdanov and H.S. Taylor, J. Phys. B 19 (1986) 4075.
[33] D. Wintgen and H. Friedrich, J. Phys. B 19 (1986) 1261.
[34] U. Fano, F. Robicheaux and A.R.P. Rau, Phys. Rev. A 37 (1988) 3655.
[35] S. Saini and D. Farelly, Phys. Rev. A 36 (1987) 3556.
[36] O. Rath and D. Richards, J. Phys. B 21 (1988) 555.
[37] H. Friedrich, Phys. Rev. A 26 (1982) 1827.
[38] H. Friedrich and M.C. Chu, Phys. Rev. A 28 (1983) 1423;
C.H. Greene, Phys. Rev. A 28 (1983) 2209;
M.-C. Chu and H. Friedrich, Phys. Rev. A 28 (1983) 3651; 29 (1984) 675.
[39] S.K. Battacharya and S.I. Chu, J. Phys. B 16 (1983) L471; 18 (1985) L275.
[40] M. Vincke and D. Baye, J. Phys. B 20 (1987) 3335.
[41] A. Alijah, doctoral Thesis, University Bielefeld (1988) unpublished.
[42] D. Wintgen and H. Friedrich, J. Phys. B 19 (1986) 991.
[43] R. Loudon, Am. J. Phys. 27 (1959) 649.
[44] M.J. Seaton, Rep. Prog. Phys. 46 (1983) 167.
[45] C.H. Greene, U. Fano and G. Strinati, Phys. Rev. A 19 (1979) 1485.
[46] H. Friedrich and D. Wintgen, Phys. Rev. A 32 (1985) 3231.
[47] D. Wintgen and H. Friedrich, Phys. Rev. A 35 (1987) 1628.
[48] E.A. Solov'ev, JETP Lett. 34 (1981) 265.
[49] C.W. Clark, Phys. Rev. A 24 (1981) 605.
[50] D. Delande and J.C. Gay, J. Phys. B 17 (1984) L335.
[51] D.R. Herrick, Phys. Rev. A 26 (1982) 323.
[52] G. Wunner, J. Phys. B 19 (1986) 1623.
[53] M.L. Zimmerman, M.M. Kash and D. Kleppner, Phys. Rev. A 45 (1980) 1092.
[54] D. Delande and J.C. Gay, Phys. Lett. A 82 (1981) 393.
[55] M.J. Englefield, Group Theory and the Coulomb Problem (Wiley, New York, 1971).
[56] W.R.S. Garton and F.S. Tomkins, Astrophys. J. 158 (1969) 839.
[57] J.C. Castro, M.L. Zimmerman, R.G. Hulet, D. Kleppner and R.R. Freeman, Phys. Rev. Lett. 45 (1980) 1780.
[58] P. Cacciani, E. Luc-Koenig, J. Pinard, C. Thomas and S. Liberman, Phys. Rev. Lett. 56 (1986) 1124; J. Phys. B 19 (1986) L519.
[59] J. Neukammer, H. Rinneberg, K. Vietzke, A. König, H. Hieronymus, M. Kohl, H.-J. Grabka and G. Wunner, Phys. Rev. Lett. 59 (1987) 2947.
[60] D. Wintgen, A. Holle, G. Wiebusch, J. Main, H. Friedrich and K.H. Welge, J. Phys. B 19 (1986) L557.
[61] A. Holle, G. Wiebusch, J. Main, K.H. Welge, G. Zeller, G. Wunner, T. Ertl and H. Ruder, Z. Phys. D 5 (1987) 279;
G. Wunner, G. Zeller, U. Woelk, W. Schweizer, R. Niemeier, F. Geyer, H. Friedrich and H. Ruder, in: Atomic Spectra and Collisions in External Fields 2, Physics of Atoms and Molecules, ed. K.T. Taylor (Plenum Press, New York, 1988);
G. Zeller, G. Wunner, R. Niemeier, H. Ruder and H. Friedrich, contribution to the Eleventh Intern. Conf. on Atomic Physics (Paris, 1988).
[62] R.A. Pullen, D. Phil. thesis, Imperial College London (1981), unpublished.
[63] M. Robnik, J. Phys. A 14 (1981) 3195.
[64] W.P. Reinhardt and D. Farelly, J. Physique Colloq. 43 suppl. 11 (1982) C2-29.
[65] A. Harada and H. Hasegawa, J. Phys. A 16 (1983) L259;
H. Hasegawa, S. Adachi and A. Harada, J. Phys. A 16 (1983) L503.
[66] J.B. Delos, S.K. Knudson and D.W. Noid, Phys. Rev. A 30 (1984) 1208.
[67] D. Wintgen and H. Friedrich, Phys. Rev. A 36 (1987) 131.
[68] D. Wintgen, J. Phys. B 20 (1987) L511.
[69] W. Schweizer, R. Niemeier, H. Friedrich, G. Wunner and H. Ruder, Phys. Rev. A 38 (1988) 1724.
[70] M.A. Al-Laithy, P.F. O'Mahony and K.T. Taylor, J. Phys. B 19 (1986) L773.
[71] M.A. Al-Laithy and C.M. Farmer, J. Phys. B 20 (1987) L747.

[72] M. Henon, in: Chaotic Behaviour of Deterministic Systems, eds G. Iooss, R.H.G. Helleman and R. Stora (North-Holland, Amsterdam, 1983) p. 53.
[73] A.J. Lichtenberg and M.A. Lieberman, Regular and Stochastic Motion (Springer, Berlin, 1981).
[74] M.C. Gutzwiller, J. Math. Phys. 18 (1977) 806.
[75] D. Wintgen and H. Marxer, Phys. Rev. Lett. 60 (1988) 971.
[76] D. Delande and J.C. Gay, Comments At. Mol. Phys. 19 (1986) 35.
[77] H.-D. Meyer, J. Chem. Phys. 84 (1986) 3147.
[78] M.A.M. de Aguiar, C.P. Malta, M. Baranger and K.T.R. Davies, Ann. Phys. (NY) 180 (1987) 167.
[79] M.C. Gutzwiller, J. Phys. Chem. 92 (1988) 3154.
[80] O. Bohigas, M. Giannoni and C. Schmit, Phys. Rev. Lett. 52 (1984) 1.
[81] N. Rosenzweig and C.E. Porter, Phys. Rev. 120 (1960) 1698.
[82] O. Bohigas and M.-J. Giannoni, in: Mathematical and Computational Methods in Nuclear Physics, Lecture Notes in Physics 209, eds J.S. Dehesa, J.M.G. Gomez and A. Polls (Springer, Berlin, 1984) p. 1.
[83] H. Köppel, W. Domcke and L.S. Cederbaum, in: Advances in Chemical Physics 57, eds I. Prigogine and S.A. Rice (Wiley, New York, 1984) p. 59.
[84] T.H. Seligman, J.J.M. Verbaarschot and M. Zirnbauer, Phys. Rev. Lett. 53 (1984) 215.
[85] M.V. Berry and M. Robnik, J. Phys. A 17 (1984) 2413.
[86] O. Bohigas, R.U. Haq and A. Panday, Phys. Rev. Lett. 54 (1985) 1645.
[87] D. Wintgen and H. Friedrich, Phys. Rev. Lett. 57 (1986) 571.
[88] D. Delande and J.C. Gay, Phys. Rev. Lett. 57 (1986) 2006.
[89] G. Wunner, U. Woelk, I. Zech, G. Zeller, T. Ertl, F. Geyer, W. Schweizer and H. Ruder, Phys. Rev. Lett. 57 (1986) 3231.
[90] D. Wintgen and H. Friedrich, Phys. Rev. A 35 (1987) 1464.
[91] A. Hönig and D. Wintgen, Phys. Rev. A 39 (1989) 5642.
[92] M.V. Berry, Proc. R. Soc. London, Ser. A 400 (1985) 229.
[93] M.V. Berry, Nonlinearity, 1 (1988) 399.
[94] J.J.M. Verbaarschot, J. Phys. A 20 (1987) 5589.
[95] T.A. Brody, Lett. Nuovo Cimento 7 (1973) 482.
[96] M.V. Berry and M. Robnik, J. Phys. A 17 (1984) 2413.
[97] A.R. Edmonds, J. Physique Colloq. 31 (1970) C4-71.
[98] A.R.P. Rau, Phys. Rev. A 16 (1977) 613.
[99] U. Fano, Phys. Rev. A 22 (1980) 226.
[100] D. Delande, C. Chardonnet, F. Biraben and J.C. Gay, J. Physique Colloq. 43 (1982) C2-97.
[101] J.A.C. Gallas, E. Gerck and R.F. O'Connell, Phys. Rev. Lett. 50 (1983) 324.
[102] M.A. Al Laithy, P.F. O'Mahony and K.T. Taylor, J. Phys. B 19 (1986) L773.
[103] D. Wintgen, Phys. Rev. Lett. 58 (1987) 1589.
[104] D. Wintgen and H. Friedrich, J. Phys. B 19 (1986) L99.
[105] W.P. Reinhardt, J. Phys. B 16 (1983) L635.
[106] E.J. Heller, Phys. Rev. A 35 (1987) 1360.
[107] M.L. Du and J.B. Delos, Phys. Rev. Lett. 58 (1987) 1731.
[108] M.L. Du and J.B. Delos, Phys. Rev. A 38 (1988) 1896, 1913.
[109] U. Eichmann, K. Richter, D. Wintgen and W. Sandner, Phys. Rev. Lett. 61 (1988) 2438.
[110] D. Wintgen, J. Phys. B 22 (1989) L5.
[111] H.C. Bryant, A. Mohaghegi, J.E. Stewart, J.B. Donahue, C.R. Quick, R.A. Reeder, V. Yuan, C.R. Hummer, W.W. Smith, S. Cohen, W.P. Reinhardt and L. Overman, Phys. Rev. Lett. 58 (1987) 2412.
[112] J.E. Stewart, H.C. Bryant, P.G. Harris, A.H. Mohaghegi, J.B. Donahue, C.R. Quick, R.A. Reeder, V. Yuan, C.R. Hummer, W.W. Smith and S. Cohen, Phys. Rev. A 38 (1988) 5628.
[113] M.L. Du and J.B. Delos, Phys. Rev. A 38 (1988) 5609.
[114] W.P. Reinhardt, in: AIP Conf. Proc., Vol. 162, ed. D.A. Micha (American Institute of Physics, New York, 1987) p. 94.
[115] J.M. Gomez Llorente, J. Zakrzewski, H.S. Taylor and K.C. Kulander, J. Chem. Phys. 89 (1988) 5959.
[116] M.C. Gutzwiller, J. Math. Phys. 8 (1967) 1979; 10 (1969) 1004; 11 (1970) 1791; 12 (1971) 343.
[117] M.C. Gutzwiller, Phys. Rev. Lett. 45 (1980) 150.
[118] M.C. Gutzwiller, Physica D 5 (1982).
[119] R. Balian and C. Bloch, Ann. Phys. (NY) 69 (1972) 76.
[120] M.V. Berry and M. Tabor, J. Phys. A 10 (1977) 371.
[121] M.V. Berry and M. Tabor, Proc. R. Soc. London Ser A 349 (1976) 101.
[122] M.V. Berry, in: Chaotic Behaviour in Deterministic Systems, eds G. Iooss, R.H.G. Helleman and R. Stora (North Holland, Amsterdam, 1983) p. 171.
[123] R.P. Feynman and A.R. Hibbs, Quantum Mechanics and Path Integrals (McGraw-Hill, New York, 1965).

[124] M.L. Du and J.B. Delos, Phys. Rev. Lett. 58 (1987) 1731.
[125] M.L. Du and J.B. Delos, Phys. Rev. A 38 (1988) 1896, 1913.
[126] E.B. Bogomolny, preprint, Landau Institute, Chernogolovka (1988);
E.B. Bogomolny, JETP Lett. 47 (1988) 526.
[127] M. Wilkinson, J. Phys. A 21 (1988) 1173.
[128] D. Wintgen, Phys. Rev. A, in preparation.
[129] P. Cvitanovic, Phys. Rev. Lett. 61 (1988) 2729.
[130] R. Aurich, M. Sieber and F. Steiner, Phys. Rev. Lett. 61 (1988) 483.
[131] D. Wintgen, Phys. Rev. Lett. 61 (1988) 1803.
[132] J. Main, A. Holle, G. Wiebusch and K.H. Welge, Z. Phys. D 6 (1987) 295.
[133] A. Holle, J. Main, G. Wiebusch, H. Rottke and K.H. Welge, Phys. Rev. Lett. 61 (1988) 161.
[134] K. Weide, K. Kühl and R. Schinke, preprint Göttingen (1989).
[135] B. Eckhardt, J. Phys. A 20 (1987) 5971.
[136] D. Wintgen and B. Eckhardt, J. Phys. B, submitted.
[137] B. Eckhardt and E. Aurell, Europhys. Lett. 9 (1989) 509.
[138] M.V. Berry, in: Lecture Notes in Physics 263 (Springer, Heidelberg, 1987) p. a1.
[139] P. Cvitanovic and B. Eckhardt, Phys. Rev. Lett. 63 (1989) 823.
[140] Q. Wang and C.H. Greene, Phys. Rev. A 40 (1989) 742.
[141] G. Wunner et al., private communication.
[142] G.R. Welch, M.M. Kash, C. Iu, L. Hsu and D. Kleppner, Phys. Rev. Lett. 62 (1989) 1975.
[143] G. Alber, Phys. Rev. A 40 (1989) 1321.
[144] S.W. McDonald and A.N. Kaufman, Phys. Rev. Lett. 42 (1979) 1189.
[145] E.J. Heller, Phys. Rev. Lett. 53 (1984) 1515.
[146] E.B. Bogomolny, Physica D 31 (1988) 169.
[147] D. Delande, private communication, to be published.
[148] D. Wintgen and A. Hönig, Phys. Rev. Lett., in press.